Title: Optogenetic scrambling of hippocampal theta oscillations alters working memory retrieval but not hippocampal spatiotemporal codes

Authors: Guillaume Etter[1,*], Suzanne van der Veldt[1], Jisoo Choi[1], Sylvain Williams[1,*]

[1]McGill University & Douglas Mental Health University Institute, Montreal, Canada

* corresponding authors: etterguillaume@gmail.com; sylvain.williams@mcgill.ca, 6875 Boulevard LaSalle, Verdun, QC H4H 1R3, Phone: 514 761-6131, Fax: 514 888-4067

Abstract:

The precise temporal coordination of activity in the brain is thought to be fundamental for memory encoding and retrieval. The medial septum (MS) provides the largest source of innervation to the hippocampus (HPC), and its inhibitory neurons play a major role in controlling HPC theta (~8 Hz) oscillations. While pharmacological inhibition of the MS is associated with memory impairment, the exact role of MS inhibitory neurons in HPC function and memory is not fully understood. While HPC place cells were previously reported to not depend on MS inputs, the exact role of MS inputs on HPC temporal codes is still a matter of debate. Moreover, pharmacological manipulations do not have the temporal resolution to distinguish the role of MS activity on working memory encoding, retention and retrieval. Here we stimulated the MS with optogenetics to either pace or ablate theta, while recording large hippocampal assemblies over time using calcium imaging along with local field potentials to monitor theta control. Using scrambled light stimulation, we could robustly ablate theta signals, which was associated with direct modulation of a subpopulation of neurons in the HPC. We found that such stimulation led to decreased working memory retrieval, but not encoding in both a delayed non-match to sample task and a novel place object recognition task. Strikingly, scrambled stimulations were not associated with disrupted spatiotemporal codes. Importantly, we show that our opsin did not transfect cholinergic cells and stimulation did not disrupt HPC ripple activity or running speed, suggesting a specific role for MS GABAergic cells in memory maintenance and retrieval that is independent from these other potential confounding mechanisms. Our study suggests that theta signals play a specific and essential role in supporting working memory retrieval and maintenance while not being necessary for hippocampal spatiotemporal codes.

Introduction

The hippocampus (HPC) plays an essential role in encoding and retrieval of episodic[1,2] and working[3] memory. While the exact physiological mechanisms of HPC-dependent memory are currently unknown, it has been proposed that HPC place cells[4] that encode specific locations of a given context could support episodic memory. In HPC subfield CA1, spatial tuning relies on contextual sensory inputs[5], but other variables such as time and distance can also be encoded in absence of sensory cues[6], likely using internal information including self-motion[7] (see McNaughton for review[8]). These time cells are a good candidate substrate for working memory[9–11] and can be identified experimentally by selectively clamping spatial cues using a treadmill or running wheel during a navigation task, and analytically using generalized linear models that implement space, time, and distance[12].

The medial septum (MS) is a neurochemically heterogeneous structure composed of GABAergic[13], mainly parvalbumin (PV)-positive neurons, along with cholinergic[14] and a smaller population of glutamatergic neurons[15,16]. The MS provides one of the major inputs to the hippocampus (HPC), and MS-PV cells project directly onto GABAergic interneurons in the HPC giving rise to feedforward inhibitory control of HPC pyramidal cells[17]. Additionally, PV interneurons within the HPC are essential in pacing theta rhythms[18], and optogenetic stimulation of MS-PV terminals in the HPC are associated with frequency specific pacing of HPC oscillations[19] whereas inhibition of the medial septum (MS) *in vivo* has been associated with reduced HPC theta rhythms[20,21]. On the other hand, MS cholinergic neurons have long been associated with episodic[22,23] memory function, rendering neurochemical differentiation essential in understanding the role of the MS in memory.

Several studies suggest that HPC theta (~8 Hz) oscillation could underlie temporal codes, since theta rhythms tightly orchestrate HPC activity[24,25]. While time cells have also been reported in both CA1 and CA3 of rodents performing tasks that do not require working memory[26], pharmacological inhibition of the MS results in specific disruption of time but not place cells and is associated with decreased working memory[27]. An important drawback of pharmacological approaches is that they do not distinguish the relative contribution of GABAergic versus cholinergic cells to memory function[28], and inhibition of MS cholinergic activity was found to alter HPC spatial representations[29] and decrease working memory performance[30,31]. Surprisingly, pharmacological inhibition of the MS was associated with reduced theta oscillation power but not place fields[32], and this resilience of place cell activity during diminished theta was not due to experience-related plasticity mechanisms[33]. In addition to encoding temporal ordering on short scales, a portion of CA1 cells remain highly stable over multiple days[34,35] while most place cells are known to be relatively unstable over long periods of time[36]. Previous attempts at inhibiting MS GABAergic interneurons specifically using optogenetics were associated with only a partial reduction, but not complete disruption of theta signals[37]. In turn, optogenetic pacing of theta oscillation has only been associated with minor changes in place cell characteristics, including a slight shift in firing frequency[38] and phase[39]. Although PV interneurons in the HPC are part of a microcircuit regulating memory consolidation[40,41], the exact role of non-cholinergic, MS-PV cells in memory encoding and retrieval remains an active area of research and has only been described recently[42–44]. Additionally, while it is hypothesized that HPC temporal codes could be directly controlled by MS inputs, causal evidence is still lacking.

Here we controlled MS activity using optogenetics to pace or ablate theta oscillations using a red-shifted excitatory opsin. We propose a novel approach to ablate HPC theta rhythms based on scrambling stimulations of MS neurons, which also allows internal controls where theta signals are paced at their natural frequency. We combined optogenetic control with calcium imaging of CA1 pyramidal cells in mice running on a linear track with sequential tones, delaying the delivery of rewards for each run. In these conditions, we were able to separate place, time, and distance cells using an information theory approach. When scrambling theta signals, our theta disruption was associated with direct activity modulation in only a small subset of CA1 pyramidal cells. While in these conditions, both place and time modulated cells were preserved, we next found that ablation of theta oscillation was associated with impaired working memory retrieval, but not encoding suggesting that MS-PV cells play a key role in generating HPC theta oscillations that are necessary for memory retrieval, but are not involved in temporal sequential activity of time modulated cells.

Results

CA1 pyramidal cells encode spatiotemporal information

To examine the spatiotemporal codes of CA1 principal cells, we injected a viral vector expressing $GCaMP6_{fast}$ under a CamKII promoter in HPC subregion CA1, implanted a GRIN lens above the injection site, and performed calcium imaging recordings of pyramidal neurons using open-source miniscopes[45,46] (fig. 1a,b; see supplemental fig. 1 for detailed histology). We extracted spatial footprints of neurons (fig. 1c) and their corresponding calcium transients (fig. 1d) using CNMFe[47]. To tease apart the spatial and temporal tuning properties of principal

cells, we used a linear track augmented with sound cues triggered by motion sensors at both ends of the track. A new sound pitch and pattern was triggered at the end of each run, informing the mice on its progression toward reward delivery and every fourth run was cued with a high pitched, continuous tone and was associated with the delivery of a reward at the end of the linear track (fig. 1e). The absolute location of each mouse, along with the time elapsed and distance traveled from departure of the reward site were monitored (fig. 1f). Using these variables and binarized neuronal activity, we computed probabilistic tuning curves (fig. 1g) and derived mutual information (MI) between neuronal activity and location, time, as well as distance for each recorded cell. In contrast to correlation based analyses, MI does not assume linear, monotonic relationships between neuronal activity and behavioral variables, but rather expresses the amount of uncertainty of one variable that can be explained by the other. The significance of MI values was tested using shuffled surrogates that underwent circular permutations (n = 1000) to preserve temporal dynamics of calcium transients and neurons that encoded exclusively one variable with a MI greater than shuffled surrogates 99.5 of the time ($p < 0.05$) were labeled as either place-modulated (spatial), time-modulated (temporal), or distance-modulated (see Methods). For the following analyses, we only focused on candidate cells that only encoded one single variable significantly (fig. 1h). Importantly, time-modulated cells were not systematically active at particular locations, and place-modulated cells were not systematically active at a given time (fig. 1i,j). While the majority of cells encoding a single variable were place-modulated, a large portion of neurons were actually conjunctive neurons that encoded more than one variable (17.98 ± 1.77 %). In contrast, cells encoding place exclusively represented 9.02 ± 1.61 % of the total recorded population, while 1.79 ± 0.68 % selectively encoded distance and 1.27 ± 0.09 % selectively encoded time (fig. 1k).

Although our information theory approach can disentangle overlapping variables by isolating cells that only significantly encode one variable, we further tested the relevance of each cell type in encoding spatiotemporal variables using a naive Bayesian classifier to decode location (fig. 1l-n), time elapsed (fig. 1o-q), and distance traveled (fig. 1r-t) on the linear track[48]. We estimated the current state of each mouse by computing the maximum *a posteriori* (MAP) value given neuronal activity and bootstrapped tuning curves computed using either actual or circularly shuffled binarized activity (fig. 1l,o,r; see Methods for detailed protocol). The quality of predictions was assessed using confusion matrices (fig. 2m,p,s) and by computing the euclidean distance between predicted state and actual state (fig. 2n,q,t). Importantly, we could only decode location using either all cells (paired *t* test, t_4 = -7.043, p = 0.0021) or place cells only (paired *t* test, t_4 = -3.780, p = 0.0194). When using any cell but place cells, we were unable to significantly decode location as decoding error was not significantly different between actual and shuffled datasets (paired *t* test, t_4 = -1.219, p = 0.2896; fig. 1n). While the number of time cells was too low to be used exclusively in our decoder for each mouse, we could only decode time successfully using all cell types (paired *t* test, t_4 = -4.908, p = 0.0079) or non-place cells (paired *t* test, t_4 = -3.540, p = 0.2402). Conversely, we were not able to decode time using place cells only (paired *t* test, t_4 = -1.682, p = 0.1677; fig. 1q), supporting that place cells identified using our method did not carry any substantial temporal codes. Finally, we could decode instantaneous distance traveled only using all cell types (paired *t* test, t_4 = -7.765, p = 0.0014), but not using only place cells (paired *t* test, t_4 = -1.416, p = 0.2295) or non place cells (paired *t* test, t_4 = -2.638, p = 0.0576; fig. 1t).

Selective MS optogenetic control of theta oscillations

To examine the relative contribution of MS-generated theta signals to HPC spatiotemporal codes, we transfected the excitatory opsin ChrimsonR in the MS (fig. 2a). In contrast to inhibitory opsins, ChrimsonR allowed us to either scramble or pace theta signals. Moreover, the advantage of the red-shifted opsin ChrimsonR over the more widely used Channelrhodopsin-2 is that it opens possibilities for combining optogenetics with calcium imaging[49]. We found virtually no expression of ChrimsonR in ChAT cells (1.05 ± 1.052 % of ChAT cells also expressed ChrimsonR; fig. 2b,c). In contrast, 14.91 ± 3.57 % of PV cells expressed ChrimsonR which we found sufficient to exert pervasive control over HPC oscillations (n = 4 mice; fig. 2d,e).

We then implanted mice with fiber optics over the MS and performed 638 nm laser stimulation while recording local field potentials (LFP) in HPC subfield CA1 (fig. 2f). We found that MS scrambled and 8 Hz stimulation could disrupt or pace theta oscillations, respectively (fig. 2g). While baseline natural theta displays some frequency variability in the 4-12 Hz frequency band, 8 Hz stimulations led to consistent and stable hippocampal oscillation at that frequency, and scrambled stimulations consistently ablated theta rhythms (fig. 2h). We found a significant interaction between our stimulation patterns and LFP frequency band (F_{10} = 6.467, p < 0.0001). In particular, scrambled stimulation significantly decreased theta power (0.341 ± 0.06 portion of baseline theta band power; p = 0.0394, pairwise t-test), while 8 Hz stimulations significantly increased theta power (3.302 ± 0.76 portion of baseline theta band power, p = 0.0004, pairwise t-test; fig. 2i) leaving other frequency bands unaltered.

HPC sharp-wave ripples (SWRs) play an essential role in memory consolidation[50–52] and stimulation of MS cholinergic neurons has been associated with reduced ripple activity[53] and impaired working memory[31]. While we found virtually no expression of ChrimsonR in MS cholinergic neurons, it was essential to measure the impact of our MS optogenetic stimulation on ripple physiology. To this end, we recorded CA1-LFP and performed 5s ON-OFF scrambled optogenetic stimulation in freely behaving mice exploring an open-field (fig. 2j). We measured attributes of ripple events before and during scrambled stimulation, and found no changes in power (t-test, $t_6 = 0.076$, $p = 0.941$; fig. 2k, left panel), frequency of occurrence (t-test, $t_6 = -1.688$, $p = 0.142$; fig. 2l, left panel), or width (t-test, $t_6 = 0.124$, $p = 0.905$; fig. 2m, left panel). Similarly, we found similar results when applying 8 Hz optogenetic stimulation when examining ripple power (t-test, $t_6 = 0.378$, $p = 0.718$; fig. 2k, right panel), frequency (t-test, $t_6 = -1.643$, $p = 0.151$; fig. 2l, right panel), and width (t-test, $t_6 = -0.138$, $p = 0.894$; fig. 2m, right panel). Together with our histological results and previous reports that optogenetic stimulation of MS cholinergic neurons reduces occurrence of SWRs[53], our findings support that our optogenetic stimulations are likely not affecting cholinergic inputs to the HPC.

Combining MS optogenetic stimulation and HPC calcium imaging

In order to study the effects of theta disruption on HPC spatial and temporal codes, we combined MS optogenetic stimulation and calcium imaging in CA1. This experimental paradigm poses two potential problems: first, the physiological state of theta oscillations following GRIN lens implants has not been studied extensively. Second, the LED used to

excite GCaMP6f could potentially activate the opsin present in MS fibers projecting to the HPC.

To verify whether GRIN lens implants had an effect on the physiology of theta, we first implanted mice with a GRIN lens in the right HPC, with two electrodes in both left and right hippocampi and found comparable theta signals in both hemispheres (fig. 3a). To gain more statistical insights, we compared theta oscillations mice with electrodes only in the right HPC, to mice with both a GRIN lens and an attached LFP electrode during open field exploration, and found no significant differences between both groups (fig. 3b). We did not find any significant difference between relative theta power to total LFP power of mice implanted with a GRIN lens and LFP electrode (0.14 ± 0.007) versus an electrode only (0.154 ± 0.008; t-test, $t_{54} = 1.060$, $p = 0.29$).

Although previous reports have already suggested that combining optogenetic stimulation of ChrimsonR at the level of cell bodies with calcium imaging of GCaMP6f at the level of terminals is possible with minimal crosstalk[49], we next controlled for any potential opsin activation of MS terminals in the HPC by recording CA1-LFP while emitting excitation light with our miniscope through a GRIN lens in mice injected with ChrimsonR in the MS. After calibrating miniscope light output power (fig. 3c), we found no effect of miniscopes blue excitation light on endogenous theta power when using excitation light power below 0.5 mW/mm^2 (1ANOVA, $F_{(4,295)} = 0.7729$, $p = 0.5435$; fig. 3d). Since it has been reported that miniscope excitation light can induce slight depolarization of terminals transfected with ChrimsonR[49], thus hindering further optogenetic-induced depolarization, we next stimulated our control mice while imaging with a ~0.3 mW/mm^2 miniscope LED power and were able to

significantly disrupt or pace theta using scrambled or 8 Hz stimulation respectively (Friedman test $\chi^2 = 6$, $p = 0.0278$; fig. 3e).

Disruption of theta rhythms modulates a small portion of CA1 cells

We then performed phasic (5s ON, 5s OFF) optogenetic stimulations of MS while recording CA1 pyramidal cells and as mice freely explored an open-field (fig. 4a). In these conditions, we found that a portion of recorded cells were consistently excited, while others were inhibited (fig. 4b; see Methods). For one representative mouse, we found that activity of pyramidal cells during stimulation was overall lower compared to baseline, for both scrambled stimulation during running (Pearson correlation, $R^2 = 0.567.$, $p < 0.0001$) and rest ($R^2 = 0.521$, $p < 0.0001$) periods, as well as for 8 Hz stimulation ($R^2 = 0.6.$, $p < 0.0001$ for rest periods; $R^2 = 0.632.$, $p < 0.0001$ for running periods; fig. 4c). Overall, ~6.42 ± 0.52 % of total cells were significantly modulated by scrambled stimulation (fig. 4d). Among those modulated cells, 50.56 ± 6.38 % were inhibited while 49.43 ± 6.38 % were excited during scrambled stimulations (n = 1849 cells, N = 5 mice; fig. 4e).

MS optogenetic stimulation alters behavior but not spatiotemporal codes

To assess the effects of theta disruption on temporal and spatial codes, we monitored HPC-CA1 pyramidal neurons' activity on the 3-tone linear track (fig. 5a). Here we leverage one of the main advantages of calcium imaging, which is the ability to register recorded cells over several days, while performing scrambled or 8 Hz stimulations on selected days (fig. 5b; fig. 5c, bottom panel). We focused our analysis on pairs of days with the exact same amount

of time (48h) between testing (fig. 5c, top panel). For each condition, we assessed the portion of total cells significantly encoding one or several variables, and found no particular effect of either 8 Hz or scrambled stimulation on spatial and temporal encoding (RM-ANOVA; F_2 = 0.807, p = 0.453 for the main effect of stimulations; F_6 = 1.283, p = 0.285 for the interaction between stimulation and encoded variable, n = 5 mice; fig. 5d).

While the portion of cells did not change under stimulation conditions, we assessed the effect of MS stimulation on place-, time-, and distance-modulated cells' tuning curves stability. To this end, we tracked neurons across days (see fig. 5c and Methods) and computed stability of place and time fields as the pairwise correlation between fields across 48h. Because CA1 is known to display prominent remapping over days[36], we also used a pair of days with no stimulation to compute a baseline stability score to be used as a reference (fig. 5e-g). We found no change in stability during MS stimulation for place-modulated cells (1ANOVA, F_2 = 1.907, p = 0.1511; fig. 5h), time-modulated cells (1ANOVA, F_2 = 2.201, p = 0.113; fig. 5i), and distance-modulated cells (1ANOVA, F_2 = 0.6962, p = 0.5024; fig. 5j).

Since a large portion of CA1 neurons encode multiple variables conjunctively, we next assessed the quality of spatiotemporal codes using random bootstrap samples (n = 100 cells per sample, n = 50 bootstrap samples) of all recorded cells. Namely, we applied a naive Bayesian classifier to decode location (fig. 6a,b), time (fig. 6c,d), and distance traveled (fig. 6e,f). For a representative mouse, decoded errors were systematically lower than shuffled surrogates, including during 8 Hz or scrambled stimulation for location (2ANOVA, $F_{1,294}$ = 543.9, $p < 0.0001$; fig. 6a), time (2ANOVA, $F_{1,294}$ = 393.7, $p < 0.0001$; fig. 6c), and distance (2ANOVA, $F_{1,294}$ = 1021, $p < 0.0001$; fig. 6e) indicating that spatiotemporal codes were preserved during stimulation. To gain statistical insights, we z-scored decoding error by using

both the actual and shuffled results (see Methods) for a given day, for every mouse (N = 5 mice; fig. 6b,d,f). MS optogenetic control did not significantly alter encoding of location (1ANOVA, $F_{2,11} = 3.8$, $p = 0.0544$; fig. 6b), time (1ANOVA, $F_{2,11} = 3.001$, $p = 0.0912$; fig. 6d), or distance (1ANOVA, $F_{2,11} = 3.398$, $p = 0.0709$; fig. 6f).

In the behavioral paradigm we use to analyze temporal modulation of neuronal activity, mice are water-scheduled and expected to collect rewards as quickly as possible. Based on this assumption, we quantified the number of returns to an empty reward site as being errors, and computed the percentage of correct runs to total runs as a proxy for performance (fig. 6g). In these conditions we found a significant effect of optogenetic stimulation on performance across days (Friedman test $\chi^2 = 6.000$, $p = 0.0278$) and in particular a significant difference in performance between during baseline (78.70 ± 2.45 %) and scrambled stimulation (44.44 ± 5.56 %; multiple comparison, $p = 0.0429$; N = 3 mice; fig. 6h). Only mice with a minimum of 12 runs were included in this analysis. Because of the limitations of this task (low cognitive load and low number of tested mice), we next set out to assess the effect of MS optogenetic stimulation in standardized behavioral tasks. Importantly, it was previously reported that pacing of theta oscillations could decrease locomotor speed and its variability[19]. In order to thoroughly assess the specificity of MS optogenetic stimulation on memory, we first sought to address potential confounding effects of our stimulation, and in particular locomotor control.

Locomotor speed dictates theta frequency, but optogenetic control does not control speed

A subset of mice injected with ChrimsonR in the MS and implanted with fiber optics in the MS and LFP electrodes in CA1 were allowed to explore an open-field freely while being subjected to 5s ON, 5s OFF optogenetic stimulations (fig. 7a). Consistently, 8 Hz stimulation led to consistent pacing of HPC oscillations to that frequency (fig. 7b). Those stimulations were not associated with any apparent change in locomotor behavior (fig. 7c), including mean speed (t-test, $t_{116} = 0.4140$, $p = 0.6796$; fig. 7d) and speed coefficient of variation (CV; t-test, $t_{116} = 0.8296$, $p = 0.4095$, n = 59 stimulation epochs; fig. 7e). Similarly, scrambled stimulation consistently led to abolished theta oscillations (fig. 7f) but no apparent changes in locomotor behavior (fig. 7g), including mean speed (t-test, $t_{118} = 0.2268$, $p = 0.8210$; fig. 7h) and speed CV (t-test, $t_{118} = 1.838$, $p = 0.686$, n = 60 stimulation epochs; fig. 7i).

While natural theta frequency and locomotor speed are correlated, the exact direction of causation between these two variables remains poorly understood. To answer this question, we performed optogenetic stimulation using a 5s ON, 5s OFF paradigm and a random frequency was selected for each stimulation epoch (fig. 7j). These stimulation frequencies covered the entirety of the theta band spectrum (fig. 7k). As expected, we found that natural theta oscillations frequencies are directly correlated to running speed for one example mouse ($R^2 = 0.1114$, $p < 0.0001$; fig. 7l). Importantly, when theta oscillation frequency is the result of MS optogenetic control, correlation drops below chance level ($R^2 = 0.0006779$, $p = 0.6244$; fig. 7m) suggesting that locomotion dictates theta frequency, but not the opposite. We systematically replicated these results across mice and observed a drop in the correlation between theta frequency and locomotor speed under optogenetic stimulation control (paired t-test, $t_3 = 3.922$, $p = 0.0295$; fig. 7n). Altogether, these results support that our optogenetic

stimulation does not alter locomotor behavior which is highly relevant for the behavioral assays we next employed.

Disruption of theta signals impairs working memory maintenance and retrieval, but not encoding

To test the role of theta signals in spatial memory, we prepared a dedicated group of mice injected with ChrimsonR and implanted with a fiber optic in the MS (fig. 8a, left panel). Mice were subjected to a novel place object recognition (NPOR) task (fig. 8a, right panel). To assess the role of theta oscillations in memory retrieval, we performed optogenetic stimulations specifically during testing and computed recognition index (RI; see Methods). In these conditions, memory performance was significantly reduced for both scrambled (0.472 ± 0.048 RI, n = 6 mice) and 8 Hz stimulations (0.435 ± 0.057 RI, n = 6 mice) groups, compared to YFP controls that displayed a significant increase in object exploration during testing (0.61 ± 0.018 RI, n = 12 mice; 2ANOVA, $p = 0.0097$; fig. 8b).

To further examine the effect of optogenetic control of the MS on specific phases of working memory function (encoding, maintenance, and retrieval), we transfected mice with ChrimsonR and implanted with fiber optics in the MS and trained them in a delayed non-match to place (DNMTP) task: briefly, in the sample phase mice were forced to run to a randomly designated arm to collect a reward. After a delay (10 s), mice could either run in the opposite arm (correct choice) to receive another reward, or run in the same arm (incorrect arm) in which case no additional reward was provided (fig. 8c). The advantage of this task is to allow for repetitive testing, specific isolation of task phases (training, delay, testing) and

within-subject controls. Mice were trained in this task with no stimulation, until criterion performance of 0.8 (portion of correct trials) was reached for at least two days. Both ChrimsonR and YFP control mice displayed significant improvement over time (RMANOVA, $F_8 = 8.737$, $p < 0.0001$ for the main effect of training days). Importantly, we found no learning rate differences between the two groups (pairwise Tukey; $p = 0.42$; fig. 8d). Once mice had learned the rule associated with the DNMTP task, we assessed performance while delivering either scrambled (0.792 ± 0.045) or 8 Hz (0.850 ± 0.036) stimulation in the encoding phase (forced choice) only, and did not observe any difference in performance compared to baseline (0.825 ± 0.030, RM-ANOVA, $F_{11} = 2.197$, $p = 0.547$, n = 12; fig. 8e). When stimulated only during the delay period, only scrambled stimulations significantly decreased memory performance (0.733 ± 0.057) compared to baseline (0.825 ± 0.030, RM-ANOVA, $F_{11} = 3.483$, $p = 0.0495$; fig. 8f). In contrast, when stimulated during retrieval, mice stimulated with 8 Hz displayed significantly reduced memory performance (0.675 ± 0.049) compared to baseline (0.825 ± 0.030, RM-ANOVA, $F_{11} = 3.265$, $p = 0.050$; fig. 8g). In contrast, YFP control mice were not affected by stimulations during encoding (RM-ANOVA, $F_2 = 0.1314$, $p = 0.8781$), the delay period (RM-ANOVA, $F_2 = 0.2020$, $p = 0.8197$), or retrieval (RM-ANOVA, $F_2 = 0.0454$, $p = 0.9557$) of working memory.

Discussion

Within the septohippocampal system, the exact causal relationships between (1) MS activity, (2) HPC oscillations, (3) HPC neuron activity, and (4) behavior including memory remains an active area of research. In particular, whether and how the MS supports encoding of place and time in the HPC, and its specific contribution to memory function is still unclear. Here, we

leveraged more recent techniques that allowed us to record >1000 neurons while performing optogenetic stimulation of MS neurons with a sub-second resolution to control theta rhythms and assess its role in hippocampal physiology and memory. Importantly, using an excitatory opsin and either scrambled or 8 Hz stimulations, we were able to consistently and robustly abolish or pace HPC theta respectively. Compared to MS inhibition, our approach enables within-subject comparison of two opposed states (paced vs abolished theta). We combined a novel behavioral apparatus which, together with information theoretical approaches, allowed us to disentangle spatial and temporal HPC codes. This method alleviates the need for arbitrary thresholds, which enables a standardized approach to calcium imaging analysis as described previously[48]. While a large portion of CA1 pyramidal neurons expressed a mixture of spatiotemporal codes, we focused our analyses on neurons tuned specifically to place, time, or distance traveled.

In our conditions, our scrambled and 8 Hz stimulations drastically abolished or paced theta rhythms respectively, and led to an overall decreased activity in a subpopulation of CA1 pyramidal cells. Our optogenetic scrambling stimulations of the MS were not associated with major changes in place cell activity, as it was reported previously with both pharmacological inhibition[27,32,33], or optogenetic[38,39] pacing of MS or septal inputs to the HPC. Importantly, our effects were likely non-cholinergic: firstly, in our immunohistological experiments we found virtually no expression of ChrimsonR in ChAT neurons of the MS. Secondly, our optogenetic stimulations were not associated with changes in hippocampal ripples, while previous reports indicate that ChAT neurons stimulation are associated with reduced ripple frequency[31,53]. As MS neurons are known to be the main driver of HPC oscillations, we expected that MS stimulation would be associated with disrupted time or distance cell activity in conditions of reduced theta rhythms, but did not observe any change for both abolished and paced theta

conditions. Additionally, pacing of HPC oscillations to 8 Hz did not lead to changes in the quality of spatial codes as reported previously[38], and did not affect temporal codes as observed in our behavioral paradigm.

While it was reported that time (but not place) cells could depend directly on medial entorhinal cortex (MEC) inputs[54], other studies show that MEC lesions do not lead to any alterations in HPC time cell physiology[55]. Importantly, a more recent investigation found that optogenetic pacing of the MS did not disrupt the spatial codes of grid cells in the entorhinal cortex[56], further suggesting that MS activity is not directly involved in spatial codes within the hippocampal formation. Together with our results, this suggests that temporal codes could either be the result of MS-dependent computations within the entorhinal cortex[56] (1), or be generated intrinsically within the HPC itself (2). While we did not examine these avenues in our current study, we posit that this could be a worthwhile hypothesis in the context of understanding time cell physiology. It is worth pointing out that previous investigation of time cells in the HPC relied on activity recorded on a treadmill, whereas our approach is based on information theoretic disentanglement, resulting in the identification of potentially different cell populations. While we were able to clearly identify a subpopulation of CA1 cells that specifically encode time (~1% of all cells), a large portion of pyramidal cells (~18%) encoded a mixture of spatial, time and distance variables suggesting that temporal codes are broadly distributed in the HPC and likely utilized as a conjunctive signal in downstream regions.

While early studies found that the MS played an essential role in maintaining time cells and supporting working memory[27], recent experimental evidence shows that the exact contribution of time cells to working memory performance could be less than previously thought[55]. Although we observed reduced memory performance when using optogenetic

stimulation during retrieval for both the novel object place recognition and the delayed non-match to place tasks, stimulation during the encoding phase was not associated with reduced memory. Importantly, we provide experimental evidence that manipulation of MS does not alter locomotor speed and that conversely, locomotor speed dictates theta frequency. This could suggest that the HPC uses different physiological modes of operation with variable dependence on theta rhythms. Even though place and time codes were preserved during our MS stimulations, a portion (~6%) of cells were directly modulated, and could account for memory impairments observed in our behavioral assays. Moreover, although we did not observe changes in frequency bands other than theta, we cannot exclude that CA1 pyramidal neuron spike timing could be drastically altered when scrambling theta oscillations, while 8 Hz stimulation were shown to not result in increased HPC activity[43], which could explain the differential effects of those stimulation patterns on working memory performance.

In summary, using calcium imaging, optogenetics, and electrophysiology, we found that theta rhythms can be paced or ablated using stimulation of the MS. These effects were non-cholinergic, and did not disrupt HPC ripple activity. Such stimulation impaired memory retrieval and maintenance, but not encoding. Finally, while a small fraction of HPC neurons respond directly to optogenetic stimulation of the MS, place, time, and distance cells were not disrupted by reduced theta oscillations. Together these results suggest that while MS input to the HPC plays an essential role in memory, time cells might not be the direct substrate for such functions.

Figure legends

Figure 1. Spatial and temporal codes are present in partially overlapping populations of CA1 neurons. a, mice were injected with GCaMP6f in hippocampal subfield CA1 and subsequently implanted with a GRIN lens over the pyramidal cell layer for miniscope imaging. **b**, post-mortem coronal section from one example mouse. blue, DAPI; green, GCaMP6f. **c**, planar projection of extracted spatial footprints from one example mouse. **d**, corresponding calcium transients from a portion of recorded cells. **e**, behavioral paradigm used to disentangle time, place, and distance coding cells (see Methods). **f**, behavioral signals from one example mouse. **g**, example pairs of neurons modulated by place (yellow), time (green), or distance (orange) along with corresponding peak activity likelihood. **h**, 3D scatter plot of the distribution of cells selectively encoding a single variable along with their associated mutual information (MI) in each dimension. Cells in black either encode more than one variable or did not encode any variable significantly more than shuffled surrogates. **i**, individual traces from one example place-modulated cell (yellow) and one example time-modulated cell (green). Vertical scale bars: 1ΔF/F. **j**, tuning curves for place, time, and distance cells, sorted by the location of peak activity likelihood for each dimension (location, time, and distance). **k**, portion of total cells (log scale) encoding for one, several, or no variables. Bayesian decoding of location (**l-n**), time (**o-q**), and distance (**r-t**). For each encoded variable, posterior probabilities are plotted with the corresponding actual state (**l,o,r**). Confusion matrices between the actual vs decoded values (**m,p,s**). Decoding errors using all cells, place cells only, or all but place cells (**n,q,t**).

Figure 2. Selective optogenetic pacing and ablation of theta oscillations. a, AAV-ChrimsonR expressing vector was injected in the MS (blue, DAPI; red, ChrimsonR) and a fiber optic was placed at the injection site (white arrow). Scale bar, 1mm. **b**, immunohistological double staining for ChrimsonR and cholinergic (ChAT+) neurons. **c**, quantification of ChrimsonR+/ChAT+ co-expressing neurons. **d**, immunohistological double staining for ChrimsonR and parvalbumin (PV+) neurons. **e**, quantification of ChrimsonR+/ChAT+ co-expressing neurons. **f**, recording configuration, with fiber optic in the MS and electrode in CA1. **g**, wavelet spectrograms before, during, and after scrambled (left, in red) and 8 Hz (right, in blue) stimulation patterns, with associated unfiltered LFP (white overlay, and black enlarged traces at the bottom). **h**, average Fourier power spectra for 60 x 5s stimulation epochs (top), and sorted power spectra for each stimulation epoch (bottom) for baseline (left, in black), scrambled (center, in red), and 8 Hz (right, in blue) stimulations in a representative mouse. **i**, group average (n = 4 mice) portion of baseline power for each stimulation pattern and every frequency band (log scale). Frequency bands: δ, 1-4 Hz; θ, 4-12 Hz; α/β, 12-30 Hz; γ_{slow}, 30-60 Hz; γ_{fast}, 60-120 Hz; HFO (high frequency oscillations), 120-250 Hz. **j**, example unfiltered trace of a ripple event during a scrambled optogenetic stimulation epoch. **k**, mean z-scored ripple power during baseline and either 8 Hz (blue) or scrambled (red) stimulations. **l**, same for mean ripple frequency of occurrence. **m**, mean ripple width.

Figure 3. GRIN lens implant does not affect theta oscillations, and enables combined calcium imaging and optogenetics. a, diagram showing recording configuration (horizontal plane), with LFP electrodes in CA1 of both hemispheres, and a GRIN lens only in the right

hemisphere (top). Example theta oscillations recorded in both hemispheres using wavelet spectrograms, raw (black) and theta filtered (red) traces. **b**, relative theta power measured in the right hemisphere of mice implanted with electrodes and GRIN lenses (blue) versus electrodes only (green). **c**, relationship between miniscope LED input value and measured nominal power (purple) as well as actual light power corrected for the surface of a GRIN lens (blue). **d**, corresponding theta power from LFP electrode attached to GRIN lens when using different miniscope LED emitting light power values (in absence of optogenetic stimulations). **e**, effects of MS optogenetic stimulations on theta oscillations during miniscope blue light emission through the lens (8AU LED power, corresponding to ~0.3mW/mm^2).

Figure 4. MS optogenetic stimulation modulates the activity of a sub-population of CA1 pyramidal cells. a, recording CA1 neurons during MS optogenetic stimulation (5s ON, 5s OFF) while simultaneously imaging CA1 neurons in mice freely exploring an open field. **b**, peristimulus time raster plot of binarized activity for pairs of excited (left) or inhibited (right) neurons. **c**, scatter plot for all pooled neurons (n = 1849 cells, N = 5 mice) of activity probability during baseline vs stimulation (red, top: scrambled; blue, bottom: 8 Hz), for both idle (left) and running (right) periods. **d**, portion of total cells significantly modulated by stimulations (N = 5 mice). **e**, portion of modulated cells that are excited (green) or inhibited (red).

Figure 5. MS optogenetic stimulation does not disrupt the stability of spatiotemporal codes. a, we recorded mice on the 3-tone linear track to identify time-, place- and

distance-modulated cells (see fig. 1 and Methods). **b**, experimental timeline. **c**, spatial footprints of neurons recorded over days and comparison scheme used to assess stability (top). Example neuron (black arrow) tracked over the 5 experimental days (bottom). **d**, portion of total cells encoding for one or several (conjunctive) variables before and during 8 Hz and scrambled stimulations (N = 5 mice). **e**, sorted place fields for identified place cells across day pairs. The first day is used as a baseline and during the other day, mice undergo 8 Hz, scrambled, or no stimulations (control treatment). Stability is computed as the pairwise correlation of fields between the two day pairs. **f**, same for time-modulated cells. **g**, same for distance-modulated cells. **h**, corresponding average stability for place-modulated cells (each dot represents a cell pooled from N = 5 mice). **i**, same for time-modulated cells. **j**, same for distance modulated cells.

Figure 6. MS optogenetic stimulation alters behavior but does not disrupt spatiotemporal codes. Using a naive Bayesian classifier, location (**a**,**b**), time elapsed (**c**,**d**), and distance traveled (**e**,**f**) were predicted from CA1 neuronal activity. **a**,**c**,**e**, decoding error (euclidean distance) for baseline, 8 Hz, and scrambled optogenetic stimulation conditions for location, time, and distance respectively (computed in a representative mouse). **b**,**d**,**f**, decoding z-score (higher values indicate better decoding compared to shuffled surrogate) for location, time, and distance respectively using N = 5 mice. **g**, example scoring of errors (purple stars) in the tone-cued linear track task. **h**, percent of correct runs during baseline, 8 Hz, and scrambled stimulations.

Figure 7. MS optogenetic stimulation does not control locomotor speed. a, mice were implanted with fiber optics in the MS after transfecting ChrimsonR, implanted with an electrode in CA1 (left), and freely explored an open field (right). **b**, average Fourier power spectra for 60 x 5s stimulation epochs (top), and sorted power spectra for each stimulation epoch (bottom) for baseline (left, in black), and 8 Hz (right, in blue) stimulations in one example mouse. **c**, peristimulus time plot of locomotor speed before and during 8 Hz MS optogenetic stimulation. Average speed in blue (line thickness indicated SEM). **d**, average locomotor speed before and during 8 Hz MS optogenetic stimulation. **e**, locomotor speed coefficient of variation (CV) before and during stimulation. **f**, average Fourier power spectra for 60 x 5s stimulation epochs (top), and sorted power spectra for each stimulation epoch (bottom) for baseline (left, in black), and scrambled (right, in red) stimulations in one example mouse. **g**, peristimulus time plot of locomotor speed before and during scrambled MS optogenetic stimulation. Average speed in red (line thickness indicated SEM). **h**, average locomotor speed before and during scrambled MS optogenetic stimulation. **i**, locomotor speed coefficient of variation (CV) before and during stimulation. **j**, random frequency generator used to pace theta oscillations at varying frequencies (see Methods). **k**, average Fourier power spectra for 400 x 5s stimulation epochs (top), and sorted power spectra for each stimulation epoch (bottom) for baseline (left, in black), and randomly selected (right, in orange) stimulations in one example mouse. **l**, relationship between locomotor speed and natural (unstimulated) theta frequency. **m**, same but during pacing of theta oscillations at varying stimulation frequencies. **n**, correlation between speed and natural (black) or controlled (orange) theta oscillations in N = 4 mice.

Figure 8. MS optogenetic stimulations disrupt maintenance and retrieval, but not encoding of episodic and working memory. a, mice were implanted with fiber optics in the MS after transfecting ChrimsonR (top). They were then subjected to the novel object place recognition task (bottom, see Methods). **b**, in this task, both scrambled (red) and 8 Hz (blue) disrupted memory performance when stimulating during the test phase. **c**, to further examine the effect of MS stimulation on memory encoding, maintenance, and retrieval, mice were trained in a delayed non-match to place (DNMTP) task in an automated T-maze. **d**, mice were trained (in absence of stimulation) to choose the correct, non-matching arm until the performance exceeded a criterion of 0.8 portion of correct choices per day, for at least two consecutive days. **e**,**f**,**g**, performance during stimulation at different phases of the task for mice injected with ChrimonR (top) or YFP controls (bottom). Red shading indicates the stimulated regions of the maze. **e**, average daily performance when performing MS stimulations during encoding only (forced choice). **f**, average daily performance when performing MS stimulations during the 10 s delay period only. **g**, average daily performance when performing MS stimulations during the retrieval only (free choice).

References

1. Scoville, W. B. & Milner, B. Loss of recent memory after bilateral hippocampal lesions. *J Neurol Neurosurg Psychiat* **20**, 11–21 (1957).
2. Penfield, W. & Milner, B. Memory deficit produced by bilateral lesions in the hippocampal zone. *AMA Arch. Neurol. Psychiatry* **79**, 475–497 (1958).
3. Jeneson, A. & Squire, L. R. Working memory, long-term memory, and medial temporal lobe function. *Learn. Mem.* **19**, 15–25 (2012).
4. O'Keefe, J. & Dostrovsky, J. The hippocampus as a spatial map. Preliminary evidence from unit activity in the freely-moving rat. *Brain Res.* **34**, 171–175 (1971).
5. Muller, R. U. & Kubie, J. L. The effects of changes in the environment on the spatial firing of hippocampal complex-spike cells. *J. Neurosci.* **7**, 1951–1968 (1987).
6. Villette, V., Malvache, A., Tressard, T., Dupuy, N. & Cossart, R. Internally recurring hippocampal sequences as a population template of spatiotemporal information. *Neuron* **88**, 357–366 (2015).
7. Samsonovich, a & McNaughton, B. L. Path integration and cognitive mapping in a continuous attractor neural network model. *J. Neurosci. Off. J. Soc. Neurosci.* **17**, 5900–20 (1997).
8. McNaughton, B. L., Battaglia, F. P., Jensen, O., Moser, E. I. & Moser, M.-B. Path integration and the neural basis of the 'cognitive map'. *Nat. Rev. Neurosci.* **7**, 663–78 (2006).
9. Eichenbaum, H. Time cells in the hippocampus: a new dimension for mapping memories. *Nat. Rev. Neurosci.* **15**, 732–744 (2014).
10. Eichenbaum, H. On the Integration of Space, Time, and Memory. *Neuron* **95**, 1007–1018 (2017).
11. Eichenbaum, H. The role of the hippocampus in navigation is memory. *J. Neurophysiol.* **117**, 1785–1796 (2017).

12. Kraus, B. J., Robinson, R. J., White, J. A., Eichenbaum, H. & Hasselmo, M. E. Hippocampal ‘time cells’: time versus path integration. *Neuron* **78**, 1090–1101 (2013).

13. Tóth, K., Freund, T. F. & Miles, R. Disinhibition of rat hippocampal pyramidal cells by GABAergic afferents from the septum. *J. Physiol.* **500**, 463–474 (1997).

14. Simon, A. P., Poindessous-Jazat, F., Dutar, P., Epelbaum, J. & Bassant, M.-H. Firing properties of anatomically identified neurons in the medial septum of anesthetized and unanesthetized restrained rats. *J. Neurosci.* **26**, 9038–9046 (2006).

15. Sotty, F. *et al.* Distinct electrophysiological properties of glutamatergic, cholinergic and GABAergic rat septohippocampal neurons: novel implications for hippocampal rhythmicity. *J. Physiol.* **551**, 927–943 (2003).

16. Manseau, F., Danik, M. & Williams, S. A functional glutamatergic neurone network in the medial septum and diagonal band area. *J. Physiol.* **566**, 865–884 (2005).

17. Unal, G., Joshi, A., Viney, T. J., Kis, V. & Somogyi, P. Synaptic targets of medial septal projections in the hippocampus and extrahippocampal cortices of the mouse. *J. Neurosci.* **35**, 15812–15826 (2015).

18. Amilhon, B. *et al.* Parvalbumin interneurons of hippocampus tune population activity at theta frequency. *Neuron* **86**, 1277–1289 (2015).

19. Bender, F. *et al.* Theta oscillations regulate the speed of locomotion via a hippocampus to lateral septum pathway. *Nat. Commun.* **6**, 8521 (2015).

20. Green, J. D. & Arduini, A. A. Hippocampal electrical activity in arousal. *J. Neurophysiol.* **17**, 533–557 (1954).

21. Mitchell, S. J., Rawlins, J. N., Steward, O. & Olton, D. S. Medial septal area lesions disrupt theta rhythm and cholinergic staining in medial entorhinal cortex and produce impaired radial arm maze behavior in rats. *J. Neurosci.* **2**, 292–302 (1982).

22. Knox, D. & Keller, S. M. Cholinergic neuronal lesions in the medial septum and vertical limb of the diagonal bands of Broca induce contextual fear memory generalization

and impair acquisition of fear extinction. *Hippocampus* **26**, 718–726 (2016).

23. Jeong, D. U. *et al.* Improvements in memory after medial septum stimulation are associated with changes in hippocampal cholinergic activity and neurogenesis. *BioMed Res. Int.* **2014**, e568587 (2014).

24. O'Keefe, J. & Recce, M. L. Phase relationship between hippocampal place units and the EEG theta rhythm. *Hippocampus* **3**, 317–330 (1993).

25. Skaggs, W. E., McNaughton, B. L., Wilson, M. A. & Barnes, C. A. Theta phase precession in hippocampal neuronal populations and the compression of temporal sequences. *Hippocampus* **6**, 149–172 (1996).

26. Salz, X. D. M. *et al.* Time cells in hippocampal area ca3. **36**, 7476–7484 (2016).

27. Wang, Y., Romani, S., Lustig, B., Leonardo, A. & Pastalkova, E. Theta sequences are essential for internally generated hippocampal firing fields. *Nat. Neurosci.* **18**, 282–288 (2015).

28. Givens, B. S. & Olton, D. S. Cholinergic and GABAergic modulation of medial septal area: Effect on working memory. *Behav. Neurosci.* **104**, 849–855 (1990).

29. Ikonen, S., McMahan, R., Gallagher, M., Eichenbaum, H. & Tanila, H. Cholinergic system regulation of spatial representation by the hippocampus. *Hippocampus* **12**, 386–397 (2002).

30. Givens, B. S., Olton, D. S. & Crawley, J. N. Galanin in the medial septal area impairs working memory. *Brain Res.* **582**, 71–77 (1992).

31. Zhang, Y. *et al.* Cholinergic suppression of hippocampal sharp-wave ripples impairs working memory. *Proc. Natl. Acad. Sci.* **118**, (2021).

32. Koenig, J., Linder, A. N., Leutgeb, J. K. & Leutgeb, S. The spatial periodicity of grid cells is not sustained during reduced theta oscillations. *Science* **332**, 592–595 (2011).

33. Brandon, M. P., Koenig, J., Leutgeb, J. K. & Leutgeb, S. New and distinct hippocampal place codes are generated in a new environment during septal inactivation.

Neuron **82**, 789–796 (2014).

34. Kinsky, N. R., Sullivan, D. W., Mau, W., Hasselmo, M. E. & Eichenbaum, H. B. Hippocampal place fields maintain a coherent and flexible map across long timescales. *Curr. Biol.* **28**, 3578-3588.e6 (2018).

35. Gonzalez, W. G., Zhang, H., Harutyunyan, A. & Lois, C. Persistence of neuronal representations through time and damage in the hippocampus. *Science* **365**, 821–825 (2019).

36. Ziv, Y. *et al.* Long-term dynamics of CA1 hippocampal place codes. *Nat. Publ. Group* **16**, 264–266 (2013).

37. Boyce, R., Glasgow, S. D., Williams, S. & Adamantidis, A. Sleep research: Causal evidence for the role of REM sleep theta rhythm in contextual memory consolidation. *Science* **352**, 812–816 (2016).

38. Zutshi, I. *et al.* Hippocampal neural circuits respond to optogenetic pacing of theta frequencies by generating accelerated oscillation frequencies. *Curr. Biol.* **28**, 1179-1188.e3 (2018).

39. Mouchati, P. R., Kloc, M. L., Holmes, G. L., White, S. L. & Barry, J. M. Optogenetic “low-theta” pacing of the septohippocampal circuit is sufficient for spatial goal finding and is influenced by behavioral state and cognitive demand. *Hippocampus* (2020) doi:10.1002/hipo.23248.

40. Xia, F. *et al.* Parvalbumin-positive interneurons mediate neocortical-hippocampal interactions that are necessary for memory consolidation. *eLife* **6**, 1–25 (2017).

41. Donato, F., Rompani, S. B. & Caroni, P. Parvalbumin-expressing basket-cell network plasticity induced by experience regulates adult learning. *Nature* **504**, 272–276 (2013).

42. Sans-Dublanc, A. *et al.* Septal GABAergic inputs to CA1 govern contextual memory retrieval. *Sci. Adv.* **6**, eaba5003 (2020).

43. Quirk, C. R. *et al.* Precisely timed theta oscillations are selectively required during the

encoding phase of memory. *Nat. Neurosci.* **24**, 1614–1627 (2021).

44. Gemzik, Z. M., Donahue, M. M. & Griffin, A. L. Optogenetic suppression of the medial septum impairs working memory maintenance. *Learn. Mem.* **28**, 361–370 (2021).

45. Aharoni, D. & Hoogland, T. M. Circuit investigations with open-source miniaturized microscopes: past, present and future. *Front. Cell. Neurosci.* **13**, (2019).

46. Ghosh, K. K. *et al.* Miniaturized integration of a fluorescence microscope. *Nat. Methods* **8**, 871–878 (2011).

47. Zhou, P. *et al.* Efficient and accurate extraction of in vivo calcium signals from microendoscopic video data. *eLife* **7**, e28728 (2018).

48. Etter, G., Manseau, F. & Williams, S. A probabilistic framework for decoding behavior from in vivo calcium imaging data. *Front. Neural Circuits* **14**, (2020).

49. Stamatakis, A. M. *et al.* Simultaneous optogenetics and cellular resolution calcium imaging during active behavior using a miniaturized microscope. *Front. Neurosci.* **12**, 1–16 (2018).

50. Buzsáki, G. Hippocampal sharp wave-ripple: A cognitive biomarker for episodic memory and planning. *Hippocampus* **25**, 1073–1188 (2015).

51. Roux, L., Hu, B., Eichler, R., Stark, E. & Buzsáki, G. Sharp wave ripples during learning stabilize the hippocampal spatial map. *Nat. Neurosci.* **20**, 845–853 (2017).

52. Fernández-Ruiz, A. *et al.* Long-duration hippocampal sharp wave ripples improve memory. *Science* **364**, 1082–1086 (2019).

53. Vandecasteele, M. *et al.* Optogenetic activation of septal cholinergic neurons suppresses sharp wave ripples and enhances theta oscillations in the hippocampus. *Proc. Natl. Acad. Sci. U. S. A.* **111**, (2014).

54. Robinson, N. T. M. *et al.* Medial entorhinal cortex selectively supports temporal coding by hippocampal neurons. *Neuron* **94**, 677-688.e6 (2017).

55. Sabariego, M. *et al.* Time cells in the hippocampus are neither dependent on medial

entorhinal cortex inputs nor necessary for spatial working memory. *Neuron* **102**, 1235-1248.e5 (2019).

56. Lepperød, M. E. *et al.* Optogenetic pacing of medial septum parvalbumin-positive cells disrupts temporal but not spatial firing in grid cells. *Sci. Adv.* **7**, eabd5684.

57. Paxinos, G. & Watson, C. The rat brain in stereotaxic coordinates. *Acad. Press Inc* 439 (1997) doi:10.1016/0166-2236(87)90017-8.

58. Mathis, A. *et al.* DeepLabCut: markerless pose estimation of user-defined body parts with deep learning. *Nat. Neurosci.* **21**, 1281–1289 (2018).

59. Nath, T. *et al.* Using DeepLabCut for 3D markerless pose estimation across species and behaviors. *Nat. Protoc.* **14**, 2152–2176 (2019).

60. Pnevmatikakis, E. A. & Giovannucci, A. NoRMCorre: An online algorithm for piecewise rigid motion correction of calcium imaging data. *J. Neurosci. Methods* **291**, 83–94 (2017).

61. Cohen, M. X. *Analyzing neural time series data: theory and practice*. (The MIT Press, 2014).

62. Sheintuch, L. *et al.* Tracking the same neurons across multiple days in ca2+ imaging data. *Cell Rep.* **21**, 1102–1115 (2017).

Methods

Animals

All procedures were approved by the McGill University Animal Care Committee and the Canadian Council on Animal Care (protocol 2015-7650). A total of n = 41 male and female (8-16 weeks old) parvalbumin-cre mice (Jackson Laboratory) were used in this study. Mice were housed individually on a 12-hour light/dark cycle at 22°C and 40% humidity with food and water ad libitum. All experiments were carried out during the light portion of the light/dark cycle.

Adeno-associated viral vectors

Adeno-associated virus AAV5.CamKII.GCaMP6f.WPRE.SV40 (Addgene # 100834, obtained from University of Pennsylvania Vector Core) was used in all calcium imaging experiments. Adeno-associated virus (AAV) of serotype *dj* (hybrid capsid created from 8 different AAV serotypes) AAVdj-hSyn-ChrimsonR-tdTomato were obtained from the Vector Core Facility at Oregon Health and Science University in Portland, Oregon. Although hSyn is a housekeeping gene, we did not observe transfection in cholinergic cells (see Results and fig. 2b-e). An eYFP construct without the ChrimsonR sequence was used as a control (termed YFP control in this manuscript).

Surgical procedures

Mice were anesthetized with isoflurane (5% induction, 0.5-1 % maintenance) and placed in a stereotaxic frame (David Kopf Instruments). Body temperature was maintained with a heating pad, eyes were hydrated with gel (Optixcare), and Carprofen (10 ml/kg) was administered

subcutaneously. The skull was completely cleared of all connective tissue and small craniotomies were performed using a dental drill for subsequent injection or implant.

Viral injections

All viral injections were performed using a glass pipette connected to a Nanoject III (Drummond) injector at a flow rate of 1 nL/second. 500 nl of AAVdj-hSyn-ChrimsonR-tdTomato (or eYFP control) was delivered into the medial septum at a rate of 1 nL/s, at the following coordinates based on reference mouse stereotaxic atlas[57] (distance from Bregma in mm): anteroposterior (AP) 0.85, mediolateral (ML) 0, dorsoventral (DV) −4.50 using a 5º angle in the ML plane. After surgery, animals were continuously monitored until recovery.

Fiber optic implant

Two weeks post-injection, mice were anesthetized for implantation following the same surgical procedure. 200 µm diameter fiber optics with ceramic ferrule (Thor labs) were implanted at the same coordinates. Implants were cemented in place using C&B-Metabond® (Patterson dental, MN). Black nail polish was applied over the dental cement to block light emission during optogenetic stimulation.

Electrode implants

An array of 7 tungsten microelectrodes (~1 MΩ impedance) was lowered in dorsal CA1 spanning through *stratum pyramidale* (pyr), *stratum radiatum* (rad) and *stratum lacunosum moleculare* (lm). Screws placed in the bone above the frontal cortex and cerebellum served as ground and reference, respectively. Following electrode, ground and reference placement, dental cement was applied to secure the implant permanently to the skull.

Implant for calcium imaging

We injected the AAV5.CamKII.GCaMP6f virus (200 nL at 1 nl.s–1) in hippocampal CA1 using the following coordinates: anteroposterior (AP) −1.86 mm from bregma, mediolateral (ML) 1.5 mm, dorsoventral (DV) 1.5 mm. 2 weeks following the injection, the mouse was anesthetized with isoflurane and the skull was cleared. A ~2 mm diameter craniotomy was performed in the skull above the injection site. An anchor screw was placed on the posterior plate above the cerebellum. The dura was removed, and the portion of the cortex above the injection site was aspirated using a vacuum pump, until the corpus callosum was visible. These fiber bundles were then gently aspirated without applying pressure on the underlying hippocampus, and a 1.8 mm diameter gradient index (GRIN; Edmund Optics) lens was lowered at the following coordinates: AP −1.86 mm from bregma, ML 1.5 mm, DV 1.2 mm. The GRIN lens was permanently attached to the skull using C&B-Metabond (Patterson Dental), and Kwik-Sil (World Precision Instruments) silicone adhesive was placed on the GRIN to protect it. 4 weeks later, the silicone cap was removed and CA1 was imaged using a miniscope mounted with an aluminum base plate while the mouse was under light anesthesia (~0.5 % isoflurane) to allow the visualization of cell activity. When a satisfying field of view was found (large neuronal assembly, visible landmarks), the base plate was cemented above

the GRIN lens, the miniscope was removed, and a plastic cap was placed on the base plate to protect the GRIN lens.

Simultaneous calcium imaging and electrophysiological recordings

To control for the effects of GRIN implants on theta physiology as well as cross-talk between miniscope and optogenetic excitation lights, we attached tungsten micro-electrodes to GRIN lenses. To this end, we placed GRIN lenses horizontally under a low-magnification microscope in a dust-free environment. A tungsten microelectrode was gently placed on the top-edge of the GRIN lens using a micromanipulator. We used the known diameter of the GRIN lens as a reference unit to estimate the desired protrusion of the electrode (~50µm, further assessed digitally after taking a microphotograph of the preparation) in accordance with our planned implantation coordinates. Small amounts (~50µL) of superglue were deposited on the top edge of the GRIN lens with the electrode in place, left to dry for ~10min, before applying the next layer of glue. 5 thin layers were used to maintain the electrode attached to the GRIN lens. After implantation of these GRIN-electrode assemblies using the protocol described above, the protruding wires were gently bent and hidden under a protective cap (1-1.5 cm high) retrieved from the pear of a manual suction pipette as a replacement for Kwik-Sil.

***In vivo* behavioral procedures**

Habituation

Mice were habituated by being gently handled for ~5 min over the course of one week, with progressive habituation to the plugging procedure (fiber optic, baseplate, and electrophysiological pre-amplified tethers. Animals were then water-scheduled (2h access per day). Miniscope recordings were performed at 30 Hz for 15 minutes, with only one recording session per day to minimize photobleaching.

Miniscope recordings

Miniscopes (V3) were assembled using open-source instructions as described previously (miniscope.org). Imaging data were acquired using a CMOS imaging sensor (Aptina, MT9V032) and multiplexed through a lightweight coaxial cable. Data was acquired using a data acquisition (DAQ) box connected via a USB host controller (Cypress, CYUSB3013). Animal behavior was recorded using a consumer grade webcam (Logitech) mounted above the environment. Calcium and behavioral data were recorded using miniscope.org open source DAQ custom acquisition software. The DAQ simultaneously acquired behavioral and cellular imaging streams at 30 Hz as uncompressed .avi files of 1000 frames, along with timestamps to enable precise temporal alignment of behavioral and calcium imaging data.

In vivo electrophysiological recordings

Following 1 week of post-surgical recovery and one week of habituation to the tethering setup, LFP from implanted mice was recorded. All recorded signals from implanted electrodes were amplified by the tether pre-amplifier before being digitized at 22 KHz using a

digital recording system (Neuralynx, USA). Recordings of each channel signal were saved in a dedicated file along with video recordings and TTL signals from the Laser Diode for subsequent analysis.

Optogenetic stimulation

Laser stimulation was delivered through a fiber optic cord (200 μm diameter) using a laser diode fiber light source (Doric Lenses). Light intensity was calibrated and wavelength-corrected using the Power Meter Bundle with the PM100D Console and S130C Slim Photodiode Sensorlight (Thorlabs). Every pacing stimulation (including 8 Hz) was performed using 5 ms square pulses. To apply scrambled light stimulation, we used an Arduino microcontroller to generate a white noise oscillation signal directly fed into the analogue input of the laser diode driver. To perform randomly selected frequency stimulation, we used a standard 5s ON, 5s OFF protocol but for each stimulation epoch, we used an Arduino microcontroller to randomly select a stimulation frequency in the theta band. When applying optogenetic stimulation during behavior, a loose piece of heat shrink tubing was fitted around the junction between the patch cord and the mouse' ferrule implant to limit visible light emission. Light intensities are expressed as nominal power, as measured at the tip of the fiber optic implant - cord assembly, and corrected for the appropriate wavelength.

Behavioral assays

Sequential tone linear track

Mice were water scheduled and could access water only for 2h per day from 6-8 pm. To disentangle spatial, temporal, and distance codes, we build a 134 cm long linear track using medium gray Lego® bricks which allows easy modifications and implementations without the need to permanently modify the structure of the maze. Pyroelectric sensors were placed in each end of the linear track, and were connected to an Arduino microcontroller. Each detection triggered a new tone in sequence, indicating the progress to reward delivery. The following tones were used and delivered using a piezo speaker: 1Hz beeps at 2,000Hz, 4Hz beeps at 3,000Hz, and a continuous tone at 4,000Hz. When the last, continuous tone was triggered, a reward (10% sucrose in water) was delivered at the starting end of the linear track in the cap of a 15 mL Falcon tube.

Novel object place recognition

On the first day, mice were allowed to freely explore a 45x45 cm dark gray open-field that contained visual cues (large white horizontal and vertical gratings) on its walls for 10 min. On the second day, two identical objects (helping hand base) were presented for 10 min. On the third day, mice were allowed to explore the same open field while the location of one of the two objects was displaced. To control for potential spatial preference biases, both the initial as well as the displaced position of objects were randomized. Mice were attributed a random testing order that was kept identical throughout the three days of testing. Behavior was recorded with a video camera and analyzed offline. Behavioral analysis was performed blind to the genotype and treatment. Object explorations were defined as epochs where mice have their nose within 1 cm of an object. Recognition index (RI) was computed as the following:

$$RI = \frac{t_{novel}}{t_{novel} + t_{familiar}}$$

where t_{novel} and $t_{familiar}$ represent the time exploring novel and familiar objects, respectively. This metric can also be computed in the sample phase for the prospectively novel (displaced) object to assess potential pre-existing preferential biases.

Automated delayed non-match to place task

Mice were water-scheduled and trained in a continuous T-maze to a delayed non-match to place task. Briefly, each trial was divided into two phases: sample and test. In the sample phase, one arm was blocked and mice were forced to explore the opposite arm where they received a 50 µL of 10% sucrose water reward. After completing the sample phase, mice were subjected to a delay (10 s). Then, during the test phase, both arms could be explored, but only the opposite (unexplored) arm is baited, so that mice have to alternate locations between sample and test phases. Mice were subjected to 10 trials (sample + test) per day, for 10 consecutive days, and the daily success rate was calculated at the number of correct choices divided by the total number of trials.

Post-mortem histological analyses

After completion of behavioral testing, mice were deeply anesthetized with a mixture ketamine/xylazine/acepromazide (100, 16, 3 mg/kg, respectively, intraperitoneal injection) and perfused transcardially with 4% paraformaldehyde (PFA) in PBS. Brains were extracted and postfixed overnight in PFA at 4 ºC and subsequently washed in PBS for an additional 24

h at 4 ºC. Brains and sections were cryoprotected in a solution of 30 % ethylene glycol, 30 % glycerol, and 40 % PBS until used. Each brain was then sectioned at 50 µm using a vibratome: every section was sequentially collected in 4 different 1.5 mL tubes to allow different analyses (electrode location, immunohistochemistry).

Immunohistology

Using one tube of collected brain sections (25% sampling) for each analysis, sections were washed 3x5 min in PBS to remove cryoprotective solution. Sections were first incubated overnight with PGT (0.45 % Gelatin and 0.25 % Triton in PBS) at 4 ºC. Next, slices were incubated with primary antibodies: either 1:200 goat anti-choline-acetyl-transferase from Millipore or 1:500 mouse anti-parvalbumin monoclonal IgG1 from Sigma-Aldrich in PGT at room temperature for 48 h or 2 h respectively. Following washes of 10, 20, and 30 min, sections were then incubated with secondary antibodies [1:2000 donkey anti-goat coupled with Alexa 488 or 1:500 goat anti-mouse IgG1 coupled to Alexa 488 (Life Technologies)] in PGT for 45 min. Following 10, 20, and 30 min washes, sections were then mounted on glass slides and permanently coverslipped with Fluoromount mounting medium that contained DAPI. Only mice with histologically confirmed placement of implants were included in this study. For GRIN lenses, the surface of the lens had to be < 100µm above *stratum pyramidale* and GCaMPf expression was confirmed using fluorescence microscopy. Electrophysiological implants had to include at least one microelectrode in CA1 *stratum radiatum* or *stratum pyramidale*. Finally, the tips of fiber optics had to be within 100 µm of the medial septum region, and proper construct expression was assessed using fluorescence microscopy.

Data analysis

Automatized tracking of behavior

To extract information about the position, velocity, and head direction of mice, we used DeepLabCut[58,59]. Briefly, we trained a model to detect mice ears, nose, body, and tailbase. Head direction was estimated using the angle between either each ear or the nose and body depending on measurement availability. Location data was interpolated to calcium imaging sampling frequency using linear interpolation. Velocity was extracted by computing $\Delta d/\Delta t$ where d is the distance and t time, and subsequently smoothed the result by applying a gaussian filter with sigma = 33 ms to remove movement artifacts. Velocity signals were used to identify periods of locomotor activity, using a threshold of 5 $cm.s^{-1}$, and used selectively to compute place, time, and distance modulation of activity.

Calcium imaging analysis

Calcium imaging data analysis was performed using MATLAB 2020a and Python 3.8.4. Video recordings were analyzed using the Miniscope Analysis pipeline (https://github.com/etterguillaume/MiniscopeAnalysis). Briefly, rigid (rotation and translation) motion correction was applied using NoRMCorre[60], and videos were spatially downsampled (3x) before concatenation. Calcium traces were extracted using CNMFe[47] using the following parameters: gSig = 3 pixels (width of gaussian kernel), gSiz = 20 pixels (approximate neuron diameter), background_model = 'ring', spatial_algorithm = 'hals',

min_corr = 0.8 (minimum pixel correlation threshold), min_PNR = 8 (minimum peak-to-noise ratio threshold).

Raw calcium traces were filtered to remove high-frequency fluctuations and binarized: briefly, neurons were considered active when normalized calcium signal amplitude > 2 standard-deviations, and first-order derivative > 0 (see Etter et al., 2020 for additional details on the methodology[48]). To extract neurons tuning to specific variables, location, time, and distance were binned (location: 3 cm bins; time: 1 s bins; distance: 3 cm bins). From binarized signals, we computed the marginal likelihood of cells being active $P(A)$ that we use as a proxy for neuronal activity. More importantly, we then derive activity likelihood, or the 'probability of being active given the state of a variable' $P(A \mid S_i)$using binned variables:

$$P(A \mid S_i) = \frac{time\ active\ while\ in\ bin\ i}{time\ in\ state}$$

where *A* is the activity level (0 or 1) of a given neuron, when being in bin *i* of a given state *S*.

To identify place, time, and distance cells, we computed the mutual information (MI) between neuronal activity and the bin *i* of a given state *S* using the following:

$$MI = \sum_{i=1}^{M} \sum_{j=1}^{2} P(S_i \cap A_j) \times log2\left(\frac{P(S_i \cap A_j)}{P(S_i) \times P(A_j)}\right)$$

where *M* is the total number of possible behavioral states, $P(S_i \cap A_j)$ is the joint probability of the animal being in bin *i* concurrently with activity level *j* (0 or 1). To assess the significance of the obtained MI value, we then generated n = 1000 shuffled surrogates using random circular permutations. We chose circular permutations because they remove the temporal relationship between neuronal activity and behavior, while still preserving the temporal structure of calcium transients and therefore leads to more conservative results (as opposed to

complete randomization of every data point, which inflates the significance value of results). Because shuffled surrogates were not systematically normally distributed, we used a non-parametric approach where the p-value (p_N) corresponds to the number of datapoints from the shuffled distribution that are greater than the actual data for each bin, divided by the number of permutations[48,61].

To determine the modulation of cells by optogenetic stimulations, we used a similar approach but computed the MI between neuronal activity and the binarized stimulation signals (thus treated as a behavioral state). The same circular shuffling procedure was then used to extract statistical significance.

Naive Bayes decoder

To further evaluate the significance of neuronal activity at the population level, we trained a naive Bayesian decoder with a uniform prior to predict spatiotemporal variables from binarized neuronal activity. The posterior probability density function, which is the probability that an animal is in a particular bin S_i, given the neural activity A is calculated using the following equation:

$$P(S_i \mid A) = \frac{P(A \mid S_i) \times P(S_i)}{P(A)}$$

where P(S|A) is the posterior probability distribution of states given neuronal activity. Using only epochs with velocity > 5 cm/s, a training dataset was generated using 50% of the data. The remaining 50% of the data was used for testing. Decoding error was calculated using 50 bootstrapped surrogates and a pool of 100 cells using randomly chosen data points with replacement. Every neuron is assumed to be independent of each other, which in practice is

not the case and leads to greater reconstruction errors, but decreases computational time. The population posterior probability was derived from the following equation:

$$P\,(S \mid A) \;=\; \prod_{k\,=\,1}^{N} \frac{P(A_k \mid S) \times P\,(S)}{P\,(A_k)}$$

with N corresponding to the number of neurons used. Finally, the decoded data point corresponds to the maximum *a posteriori* (MAP):

$$\hat{y} = \; arg\,max\,exp\left[\sum_{k\,=1}^{N} \; log(\,1 + \frac{P(A_k \mid S) \times P(S)}{P(A_k)}\,) \; - \; 1\right]$$

The exponential-logarithm trick is used to prevent underflow when multiplying a large number of small probabilities, which is a correct approximation since the posterior is a smooth convex function.

While many studies utilize temporal smoothing, we did not use any here since we want to observe the unaltered temporal codes of time-modulated cells, and temporal smoothing can lead to displacement of tuning curves[48]. On the linear track, decoding error was assessed as:

$$decoding\;error \;=\; |\,decoded\;state \;-\; actual\;state\,|$$

In order to compare decoding scores across animals, we z-scored decoding errors using the following equation:

$$z \;=\frac{\bar{x}-\bar{s}}{\sigma(x)}$$

where $\bar{x}$ is the average actual decoding error, $\bar{s}$ is the average decoding error using shuffled surrogates, and $\sigma(x)$ is the standard deviation of the actual decoding error.

Tracking cells over multiple days

Neurons were tracked over multiple days using a probabilistic method as previously described[62]. Briefly, spatial footprints were aligned using rigid alignment to correct for rotations and translations. After alignment, we considered candidate sets of cells to be the same neuron if their maximal distance was < 12 um, and used the modeled spatial correlation threshold (usually in the range .6 - .8) to determine the identity of cell pairs across days. Finally, we assessed the stability of the spatial representation using pairwise field correlation (Pearson correlation of tuning curves).

Electrophysiological analysis

Electrophysiological data analysis was performed using MATLAB 2020a and both the signal processing as well as the wavelet toolbox. Wavelet convolution was applied to LFP signals using complex Morlet wavelets ('cmor1-1.5' in MATLAB) when both time- and frequency-domain accuracy was required. Moving window Fourier convolution (2 s window in the theta band, 5 s window in the gamma band, 10 ms moving steps) was used when frequency-domain accuracy was privileged over time-domain accuracy (e.g. to plot dominant frequency when pacing using optogenetics).

Statistics

Unless stated otherwise, all data are presented as mean ± standard error of the mean (SEM) and statistical test details are described in the corresponding results. Normality distribution of each group was assessed using Shapiro-Wilk normality test and parametric tests were used

only when distributions were found normal (non-parametric tests are described where applicable). 1ANOVA: one-way ANOVA; 2ANOVA: two-way ANOVA; RM-ANOVA: repeated measure ANOVA. $p < 0.05$ was considered statistically significant. *, $p < 0.05$; **, $p < 0.01$; ***, $p < 0.001$, ****, $p < 0.0001$.

Author information

Affiliations

McGill University & Douglas Mental Health University Institute, Montreal, Canada

Corresponding authors: sylvain.williams@mcgill.ca, etterguillaume@gmail.com

6875 Boulevard LaSalle, Verdun, QC H4H 1R3, Phone : 514 761-6131, Fax: 514 888-4067

Contributions

GE and SW designed the study. GE performed and analyzed *in vivo* experiments. SVDV performed and analyzed both behavioral as well as immunohistological experiments. JC performed surgeries for the mice used for controlling cross-talk between calcium imaging and optogenetics. GE and SW wrote the manuscript with inputs from all collaborators.

Competing interests

The authors declare no competing interests.

Correspondence author

Correspondence should be addressed to Sylvain Williams: sylvain.williams@mcgill.ca

Acknowledgements: We thank Ke Cui for helping to maintain the colony and perfusing mice, and Mark P Brandon for comments on the manuscript.

Funding

This work was supported by funding from the Canadian Institutes for Health Research (CIHR), Fonds de la Recherche en Santé du Québec (FRSQ), and the Natural Sciences and Engineering Research Council of Canada (NSERC). SVDV was supported by a Vanier Canada Graduate Scholarship.

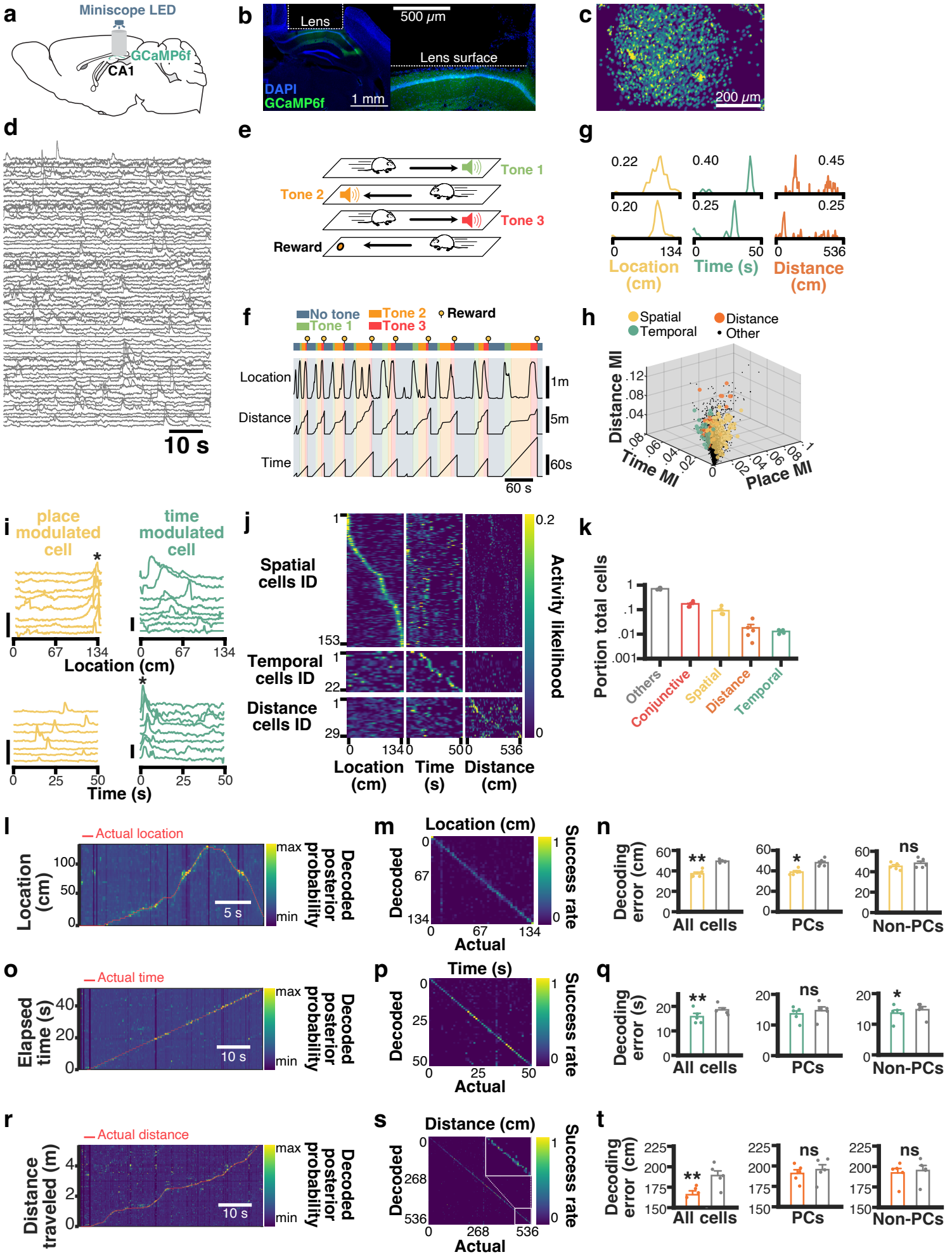
a
Miniscope LED
GCaMP6f
CA1
b
Lens
500 μm
Lens surface
DAPI
GCaMP6f
1 mm
c
200 μm
d
10 s
e
Tone 1
Tone 2
Tone 3
Reward
g
0.22
0.40
0.45
0.20
0.25
0.25
0
134
0
50
0
536
Location (cm)
Time (s)
Distance (cm)
f
No tone
Tone 1
Tone 2
Tone 3
Reward
Location
Distance
Time
1m
5m
60s
60 s
h
Spatial
Temporal
Distance
Other
Distance MI
Time MI
Place MI
i
place modulated cell
time modulated cell
Location (cm)
Time (s)
j
Spatial cells ID
Temporal cells ID
Distance cells ID
Activity likelihood
Location (cm)
Time (s)
Distance (cm)
k
Portion total cells
Others
Conjunctive
Spatial
Distance
Temporal
l
Actual location
Location (cm)
5 s
max
min
Decoded posterior probability
m
Location (cm)
Decoded
Actual
Success rate
n
Decoding error (cm)
All cells
PCs
Non-PCs
ns
o
Actual time
Elapsed time (s)
10 s
p
Time (s)
q
Decoding error (s)
r
Actual distance
Distance traveled (m)
s
Distance (cm)
t

FIGURE 1

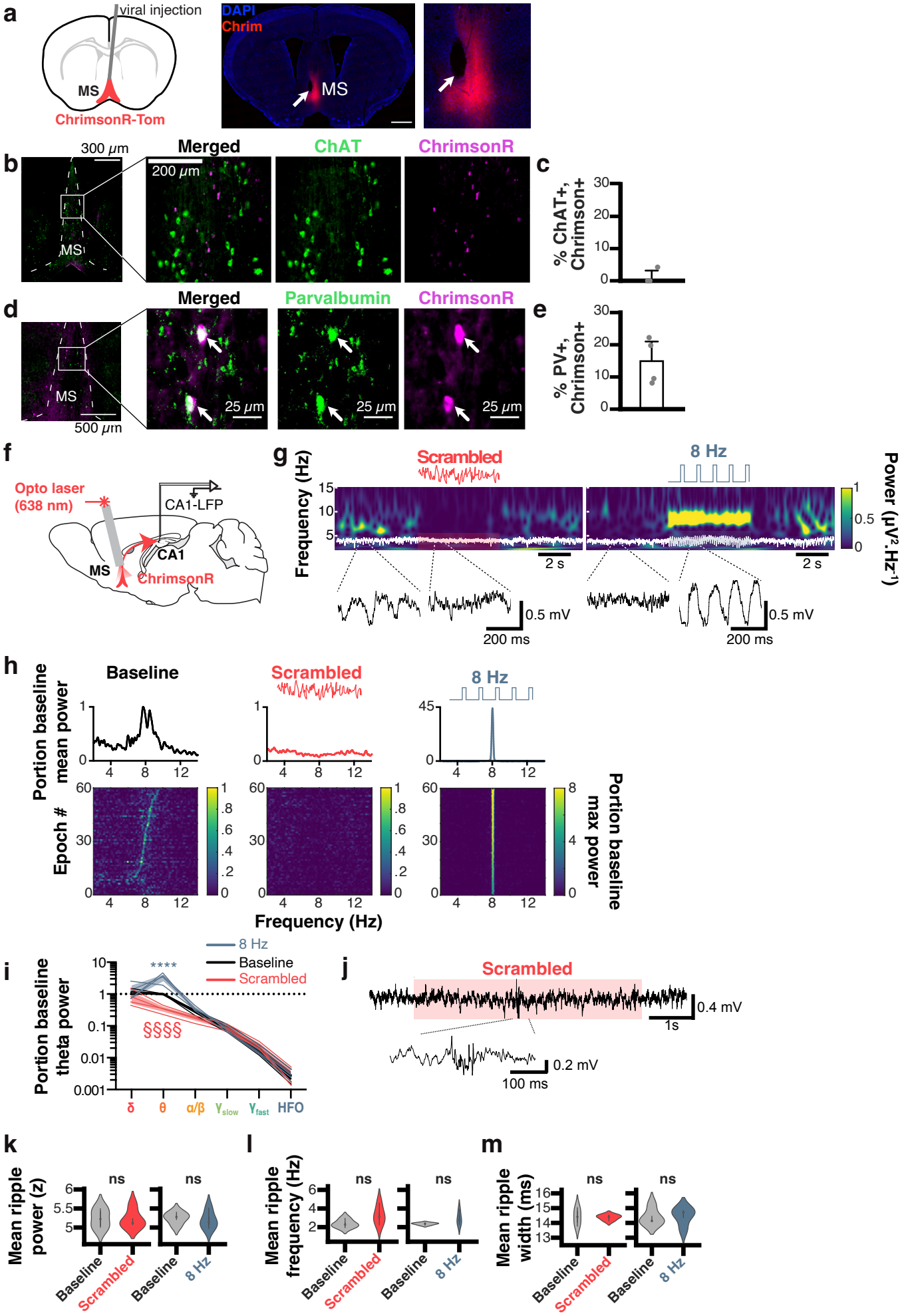
a
viral injection
MS
ChrimsonR-Tom
DAPI
Chrim
MS
b
300 μm
Merged
ChAT
ChrimsonR
200 μm
MS
c
% ChAT+, Chrimson+
30
20
10
0
d
Merged
Parvalbumin
ChrimsonR
MS
500 μm
25 μm
25 μm
25 μm
e
% PV+, Chrimson+
30
20
10
0
f
Opto laser (638 nm)
CA1-LFP
CA1
MS
ChrimsonR
g
Scrambled
8 Hz
Frequency (Hz)
15
10
5
2 s
2 s
Power (μV².Hz⁻¹)
1
0.5
0
0.5 mV
200 ms
0.5 mV
200 ms
h
Baseline
Scrambled
8 Hz
Portion baseline mean power
1
0
45
0
4
8
12
Epoch #
60
30
0
1
.8
.6
.4
.2
0
8
4
0
Portion baseline max power
Frequency (Hz)
i
8 Hz
Baseline
Scrambled
Portion baseline theta power
10
1
0.1
0.01
0.001
****
§§§§
δ
θ
α/β
γslow
γfast
HFO
j
Scrambled
0.4 mV
1s
0.2 mV
100 ms
k
Mean ripple power (z)
6
5.5
5
ns
ns
Baseline
Scrambled
Baseline
8 Hz
l
Mean ripple frequency (Hz)
6
4
2
ns
ns
Baseline
Scrambled
Baseline
8 Hz
m
Mean ripple width (ms)
16
15
14
13
ns
ns
Baseline
Scrambled
Baseline
8 Hz

FIGURE 2

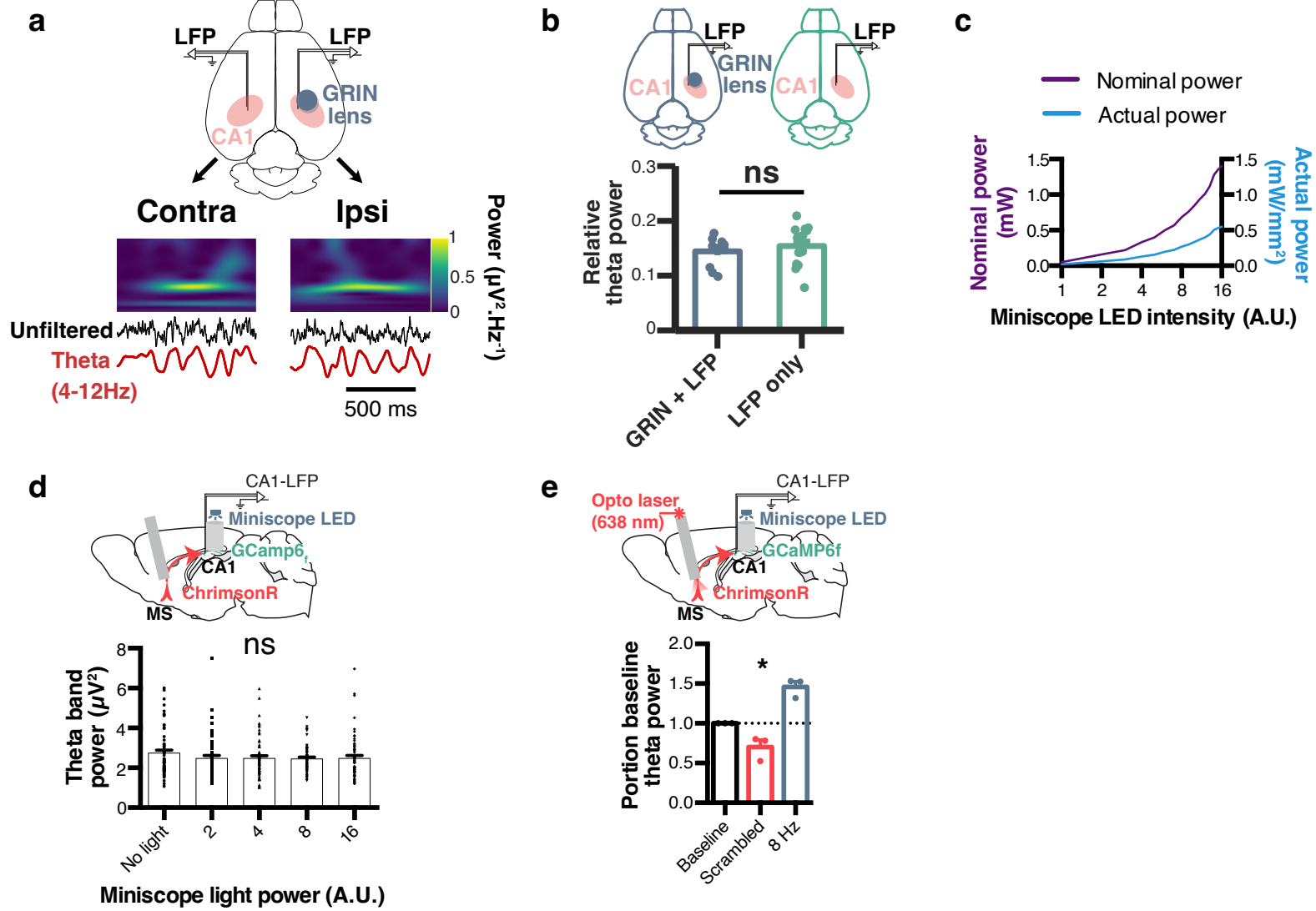
a
LFP
LFP
GRIN lens
CA1
Contra
Ipsi
Power (μV².Hz⁻¹)
1
0.5
0
Unfiltered
Theta (4-12Hz)
500 ms
b
LFP
LFP
GRIN lens
CA1
CA1
ns
Relative theta power
0.3
0.2
0.1
0
GRIN + LFP
LFP only
c
Nominal power
Actual power
Nominal power (mW)
Actual power (mW/mm²)
1.5
1.0
0.5
0.0
1
2
4
8
16
Miniscope LED intensity (A.U.)
d
CA1-LFP
Miniscope LED
GCamp6f
CA1
ChrimsonR
MS
ns
Theta band power (μV²)
8
6
4
2
0
No light
2
4
8
16
Miniscope light power (A.U.)
e
Opto laser (638 nm)
CA1-LFP
Miniscope LED
GCaMP6f
CA1
ChrimsonR
MS
*
Portion baseline theta power
2.0
1.5
1.0
0.5
0.0
Baseline
Scrambled
8 Hz

FIGURE 3

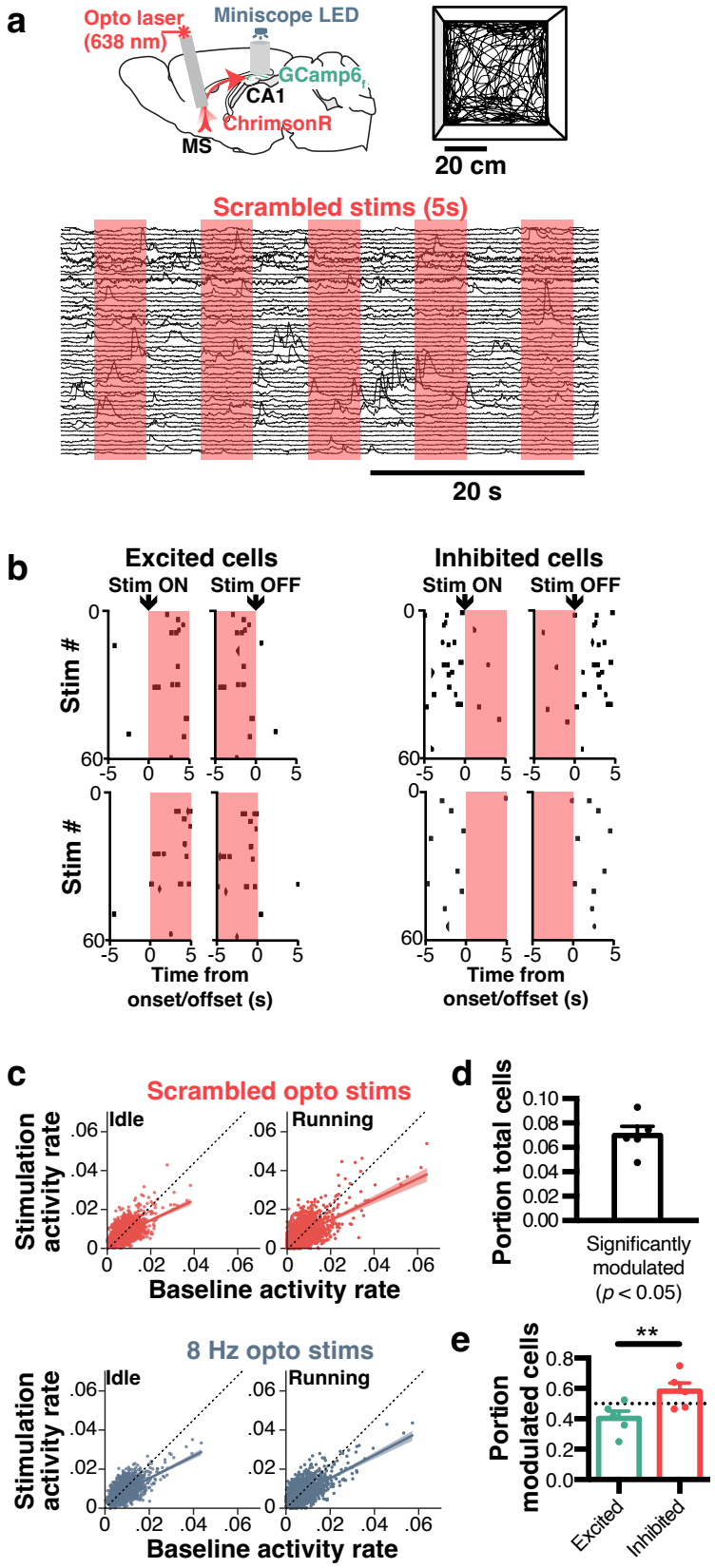
a
Opto laser (638 nm)
Miniscope LED
GCamp6f
CA1
ChrimsonR
MS
20 cm
Scrambled stims (5s)
20 s
b
Excited cells
Inhibited cells
Stim ON
Stim OFF
Stim #
Time from onset/offset (s)
c
Scrambled opto stims
Idle
Running
Stimulation activity rate
Baseline activity rate
8 Hz opto stims
d
Portion total cells
Significantly modulated ($p < 0.05$)
e
Portion modulated cells
**
Excited
Inhibited

FIGURE 4

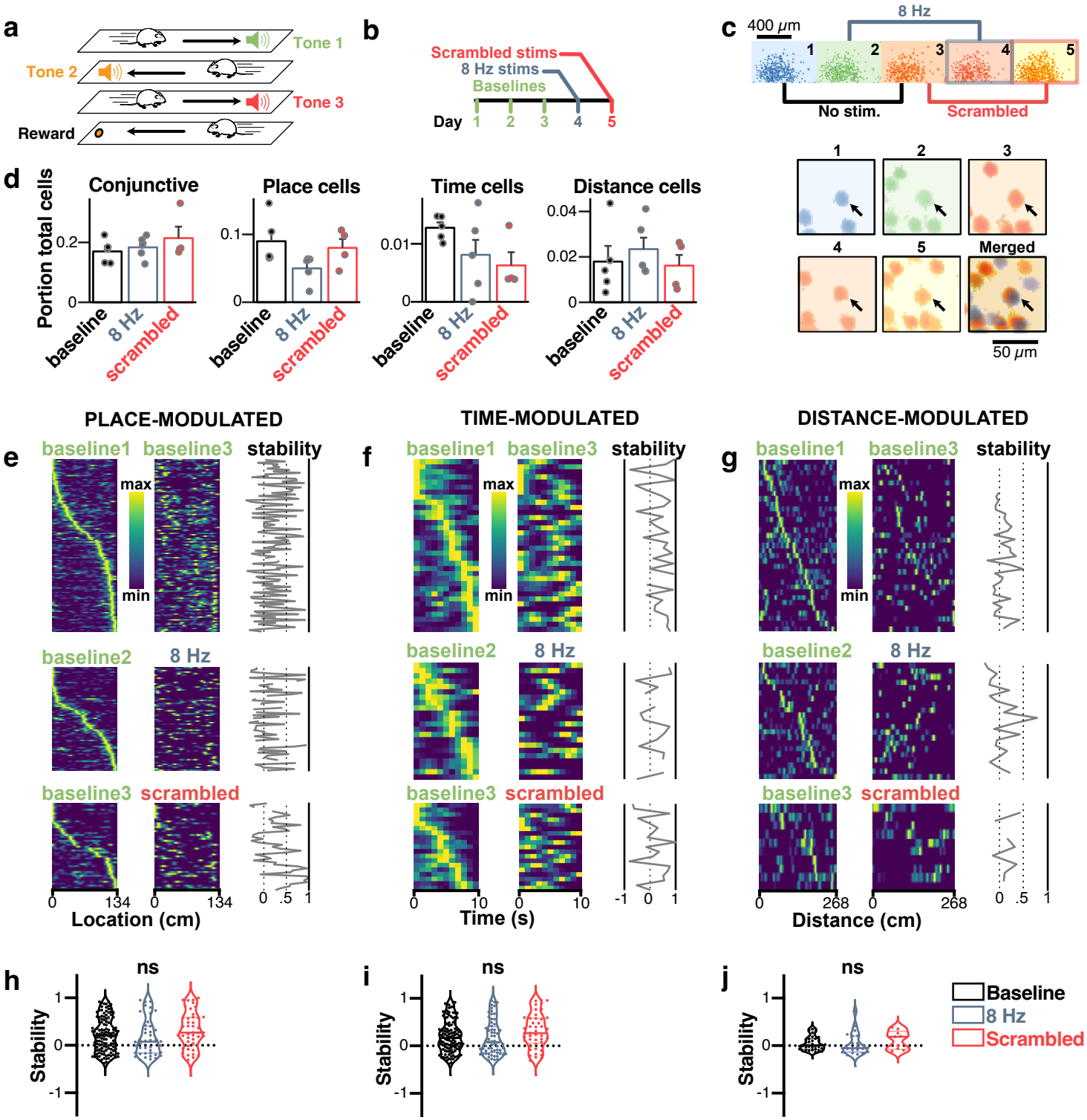
a
Tone 1
Tone 2
Tone 3
Reward
b
Scrambled stims
8 Hz stims
Baselines
Day 1 2 3 4 5
c
400 μm
8 Hz
1 2 3 4 5
No stim.
Scrambled
1 2 3
4 5 Merged
50 μm
d
Portion total cells
Conjunctive
Place cells
Time cells
Distance cells
baseline
8 Hz
scrambled
PLACE-MODULATED
TIME-MODULATED
DISTANCE-MODULATED
e
f
g
baseline1
baseline3
stability
max
min
baseline2
8 Hz
baseline3
scrambled
Location (cm)
Time (s)
Distance (cm)
h
i
j
ns
Stability
Baseline
8 Hz
Scrambled

FIGURE 5

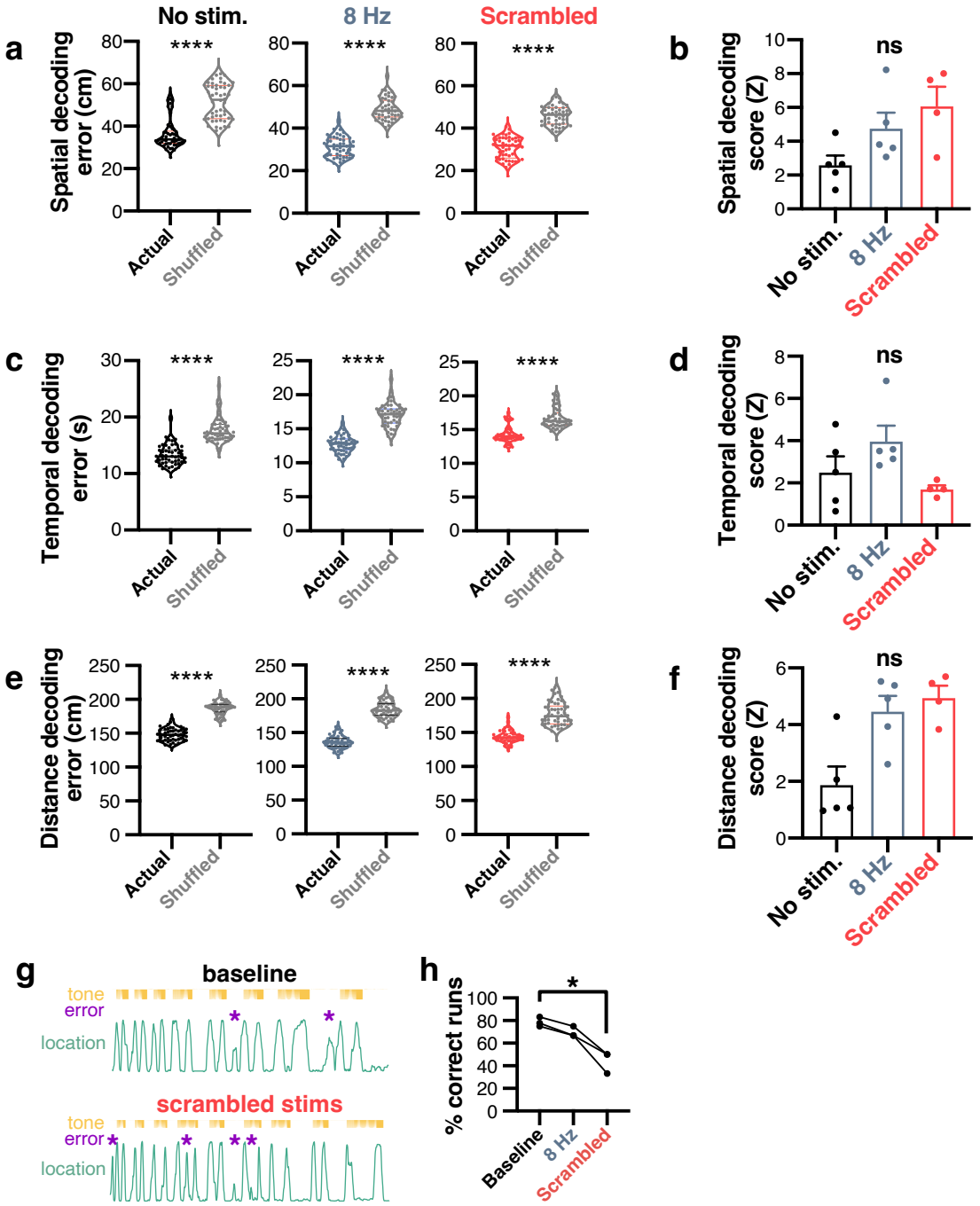
a
No stim.
8 Hz
Scrambled
Spatial decoding error (cm)
****
Actual
Shuffled
b
Spatial decoding score (Z)
ns
No stim.
8 Hz
Scrambled
c
Temporal decoding error (s)
d
Temporal decoding score (Z)
e
Distance decoding error (cm)
f
Distance decoding score (Z)
g
baseline
tone
error
location
scrambled stims
h
% correct runs
*
Baseline
8 Hz
Scrambled

FIGURE 6

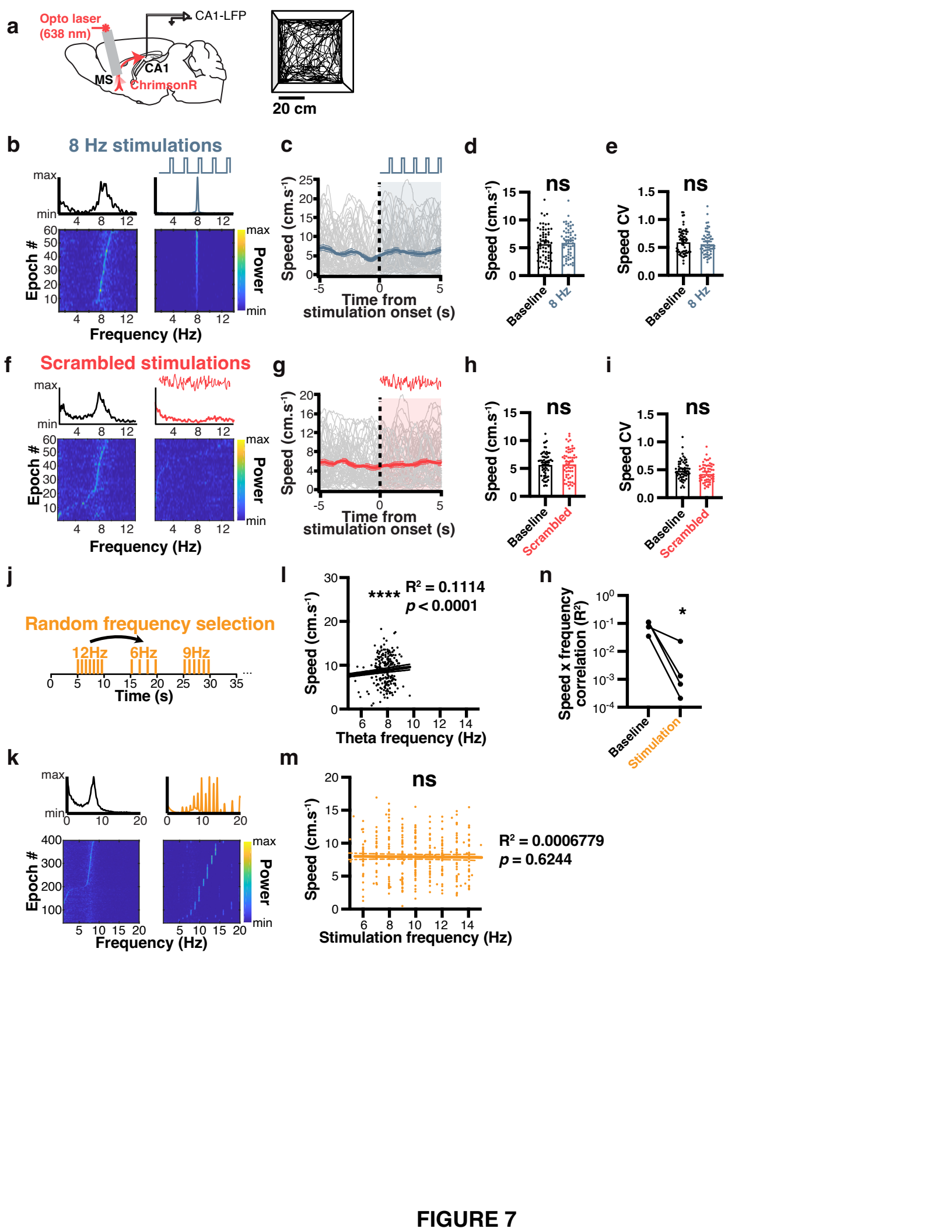
a
Opto laser
(638 nm)
CA1-LFP
CA1
MS
ChrimsonR
20 cm
b
8 Hz stimulations
max
min
Epoch #
Frequency (Hz)
Power
c
Speed (cm.s-1)
Time from
stimulation onset (s)
d
ns
Speed (cm.s-1)
Baseline
8 Hz
e
ns
Speed CV
Baseline
8 Hz
f
Scrambled stimulations
g
h
ns
Baseline
Scrambled
i
ns
j
Random frequency selection
12Hz
6Hz
9Hz
Time (s)
l
****
R² = 0.1114
p < 0.0001
Theta frequency (Hz)
n
Speed x frequency correlation (R²)
*
Baseline
Stimulation
k
m
ns
R² = 0.0006779
p = 0.6244
Stimulation frequency (Hz)

FIGURE 7

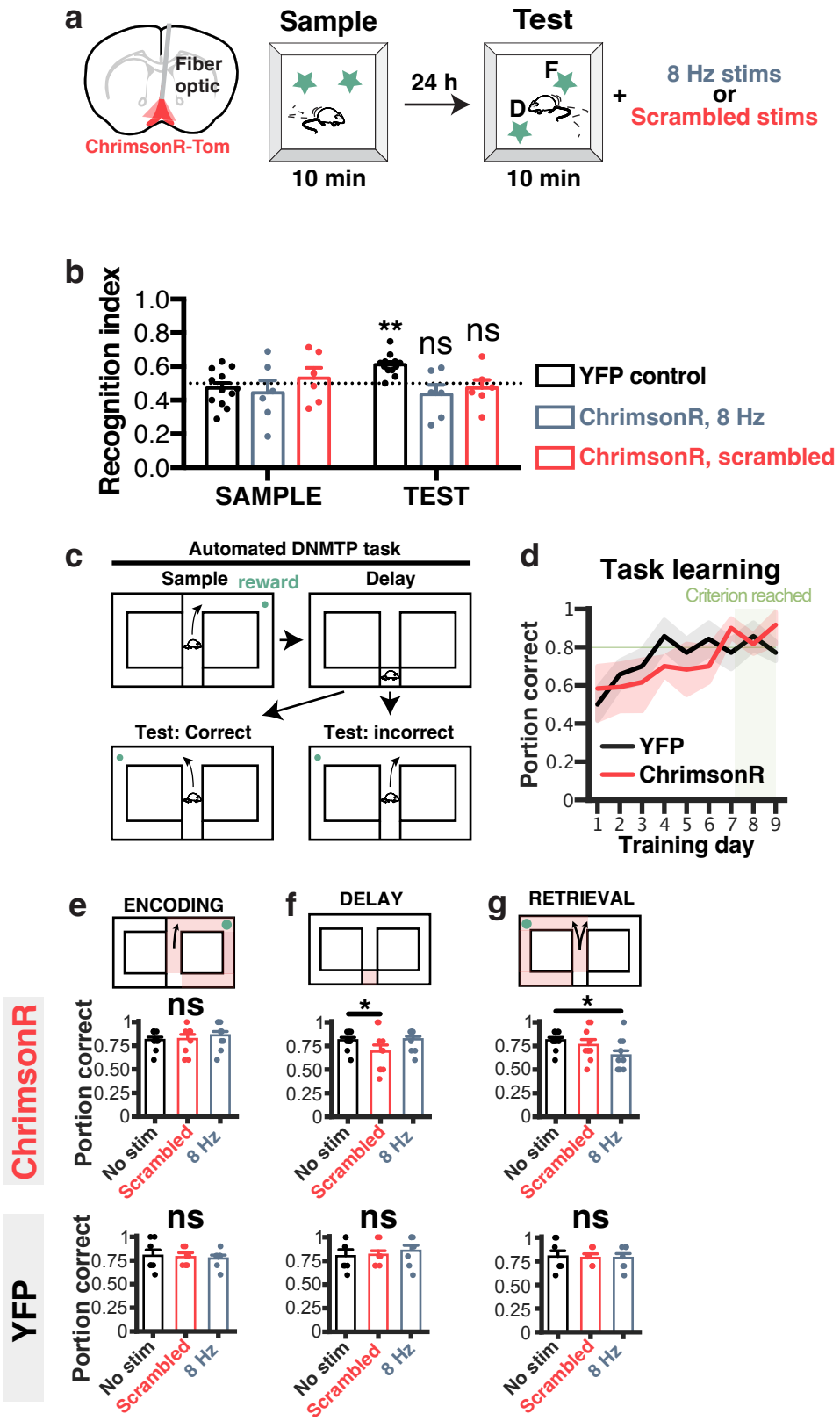
a
Fiber optic
ChrimsonR-Tom
Sample
10 min
24 h
Test
F
D
10 min
+
8 Hz stims
or
Scrambled stims
b
Recognition index
1.0
0.8
0.6
0.4
0.2
0.0
**
ns
ns
SAMPLE
TEST
YFP control
ChrimsonR, 8 Hz
ChrimsonR, scrambled
c
Automated DNMTP task
Sample
reward
Delay
Test: Correct
Test: incorrect
d
Task learning
Criterion reached
Portion correct
YFP
ChrimsonR
Training day
e
ENCODING
f
DELAY
g
RETRIEVAL
ChrimsonR
YFP
Portion correct
ns
*
No stim
Scrambled
8 Hz

FIGURE 8